Advances in material and friction data for modelling of metal machining

Shreyes N Melkote, Wit Grzesik, José Outeiro, Joel Rech, Volker Schulze, Helmi Attia, Pedro J. Arrazola, Rachid M'Saoubi, Christopher Saldana

Advances in material and friction data for modelling of metal machining

Shreyes N. Melkote (2)[a,*], Wit Grzesik (2)[b], Jose Outeiro (2)[c], Joel Rech [d], Volker Schulze (2)[e], Helmi Attia (1)[f], Pedro-J. Arrazola (2)[g], Rachid M'Saoubi (1)[h], Christopher Saldana [a]

[a] George W. Woodruff School of Mechanical Engineering, Georgia Institute of Technology, Atlanta, Georgia, 30332-0405, USA
[b] Department of Manufacturing Engineering & Production Automation, Opole University of Technology, 5th Mikolajczyka St., 45-271, Opole, Poland
[c] LaBoMaP Laboratory, ARTS & METIERS, Campus of Cluny, Rue Porte de Paris, F-71250, Cluny, France
[d] ENISE (École Associée à l'Ecole Centrale de Lyon), 58 Rue Jean Parot, 42000, Saint-Etienne, France
[e] Institute for Production Science, Karlsruhe Institute of Technology (KIT), Kaiserstraße 12, 76131, Karlsruhe, Germany
[f] Aerospace Structures, Materials and Manufacturing Laboratory, National Research Council of Canada/McGill University, Montreal, QC, H3T 2B2, Canada
[g] Faculty of Engineering, Mondragon University, Mondragón, 20500, Spain
[h] R&D Materials and Technology Development, Seco Tools AB, SE-73782 Fagersta, Sweden

Keywords:
Machining
Modelling
Friction

A B S T R A C T

This paper reviews recent advances in constitutive and friction data and models for simulation of metal machining. Phenomenological and physically-based constitutive models commonly used in machining simulations are presented and discussed. Other topics include experimental techniques for acquiring data necessary to identify the constitutive model parameters, and recent advances in modelling of tool-workpiece friction and experimental techniques to acquire friction data under machining conditions. Additionally, thermo-physical properties for thermal modelling of the machining process, and microstructure data for the chip and workpiece together with relevant experimental methods are discussed. Future research needs in each of the focused areas are highlighted.

1. Introduction

Industrial machining processes are among the most complex manufacturing processes to model and simulate. In metal cutting, the complexities stem from the severe plastic deformation of the metal, and from the extreme tribological conditions present at the tool-workpiece interfaces [207]. The ability to accurately model and simulate cutting processes such as turning, milling, etc. depends on the availability of accurate mathematical models for (i) the constitutive response of the deforming material, i.e., a *constitutive model* that describes how the material yield strength and fracture behaviour change with deformation parameters such as strain, strain rate, temperature, microstructure, etc., and (ii) the friction at the tool and workpiece interfaces, i.e., *friction model*.

A major challenge in developing constitutive and friction models for metal cutting is the difficulty in acquiring dynamic stress–strain data and friction data, respectively, that accurately represent the cutting process. Historically, metal cutting modelling and simulation efforts have relied on stress-strain data derived from quasi-static and/or dynamic materials testing to calibrate constitutive models [107]. These data and associated constitutive models usually cover a limited range of strains, strain rates, and temperatures compared to those occurring in metal cutting. Consequently, the use of such constitutive models in machining simulations generally requires *extrapolation* to higher strains and strain rates, which contributes to inaccuracies in the simulated results. In the case of friction modelling, highly simplified friction models (e.g. Coulomb friction) are often used in machining simulations. The main reasons for this include limited knowledge of the complex frictional interactions at the tool-work interfaces, and a lack of suitable experimental techniques for measuring the relevant friction model parameters under conditions representative of metal cutting.

Other types of data critical for machining process modelling and simulation include temperature-dependent thermo-physical properties and workpiece microstructure data, which are often difficult to find or measure, for the materials and deformation conditions of interest. For instance, recent microstructure evolution dependent constitutive models for metal machining require microstructure data (e.g. grain size evolution as a function of strain, strain rate, and temperature) that are not readily available for many work materials of practical interest [144].

The objective of this keynote paper is to review and critically analyse recent advances and needs in material, friction, thermal, and microstructure data and associated models, along with experimental techniques for generating the data needed for accurately simulating the metal cutting process.

The paper is organized as follows. Section 2 discusses key aspects of constitutive data and models for metal cutting including phenomenological and physically based constitutive models,

* Corresponding author at: Georgia Institute of Technology, George W. Woodruff School of Mechanical Engineering, 813 Ferst Drive, N.W. Rm. 381, MARC, Atlanta, Georgia 30332-0405, United States. Fax: 01 404 894 9342.
E-mail address: shreyes.melkote@me.gatech.edu (S.N. Melkote).

experimental techniques for generating the data required to fit the constitutive model parameters, methods for model parameter identification, a critical assessment of the data and models, and future research needs and opportunities. Section 3 reviews key aspects of friction in metal cutting, friction models and associated data requirements, and experimental methods for generating the friction data. Section 4 reviews thermal aspects of metal cutting, and the pertinent models and data. Section 5 reviews microstructure evolution in metal cutting, experimental methods for generating relevant microstructure data, and associated models. Section 6 concludes with a summary of the paper and a future outlook.

2. Constitutive data and models

2.1. Deformation characteristics in machining

2.1.1. Strains, strain rates, and temperatures

Metal machining is a severe plastic deformation process characterized by heterogeneous thermomechanical deformation of the metal at high deformation rates leading to the modification of the microstructure and material properties. Consequently, constitutive modelling for metal machining requires fundamental understanding of the deformation conditions in the relevant deformation zones (Fig. 1).

Accurate knowledge of the strains, strain rates, and temperatures are critical for understanding and controlling the machining process. Large strains (1–10), strain-rates (up to 10^6 s^{-1}) and temperatures (>1000 °C) are reported in metal cutting [10]. However, it should be noted that the large strains and strain-rates reported are often estimated using simplified shear plane based analytical models, which weren't validated using suitable experimental techniques capable of measuring such values under practical cutting conditions. Moreover, large temperatures are reported in the secondary deformation zone. In addition, the mechanical behaviour of the work material in machining also depends on other parameters such as the microstructure (e.g., dislocation density, grain size, etc.) [144] and the state-of-stress [27]. Therefore, proper identification of the deformation conditions and their ranges in metal cutting is essential for the design and selection of suitable mechanical tests to characterize the work material behaviour under conditions representative of metal cutting.

In-situ experimental techniques such as Particle Imaging Velocimetry (PIV) have been used to characterize the strain and strain-rate distributions in metal cutting [139]. In this technique, heterogeneous surface markers in the workpiece surface are tracked using high-speed imaging (Fig. 3). The strain fields are calculated using the relative displacements of the heterogeneous surface markers.

Using PIV, Brown et al. [37] estimated a strain-rate of ~20 s^{-1} in the primary shear zone and a shear strain of 2.05 in a OFHC copper chip at a very low cutting speed of 0.3 m/min. In order to estimate the strain and strain-rate, they used a classical shear plane based analytical model. Huang et al. [113] performed similar experiments

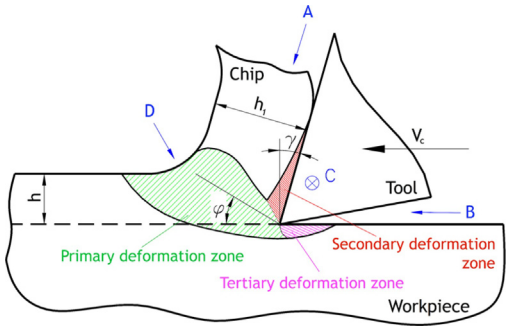

Fig. 1. Deformation zones in the metal cutting process.

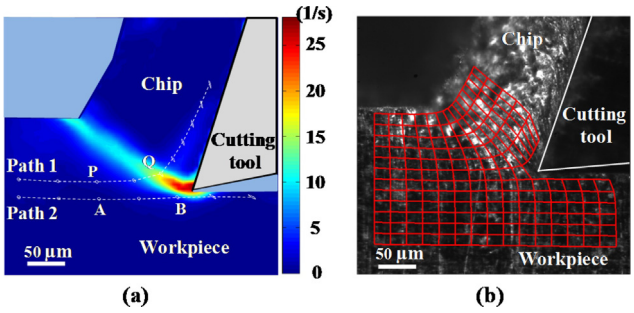

Fig. 2. PIV technique used to characterize deformation in machining: (a) Effective strain rate field, (b) Grid distortion [102].

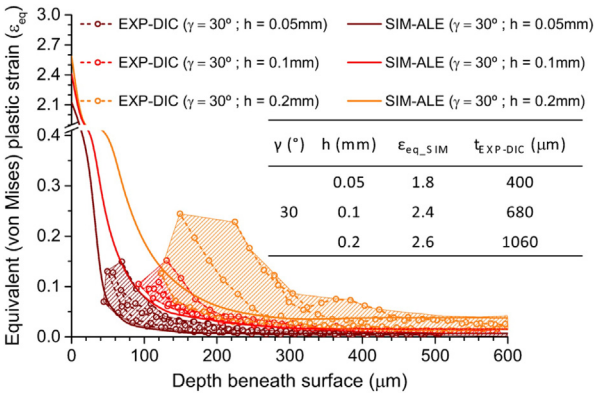

Fig. 3. Measured and predicted through-depth plastic strain distributions at different uncut chip thicknesses [167].

on Ti–6Al–4V at a comparable low cutting speed of 0.6 m/min and they estimated strain-rates of ~40–80 s^{-1} and a strain of ~1.5.

In general, the PIV technique is restricted to measurements at low cutting speeds due to imaging speed limitations. Nevertheless, it is a very useful in-situ technique to understand and quantify the deformation field in metal cutting.

Recently, Sagapuram [194] used high speed imaging to investigate the mechanism of shear-localized chip formation in orthogonal cutting of Ti–6Al–4V at cutting speeds of 0.25 m/s–5 m/s. Using a combination of marker displacement techniques and microscopy, they estimated the average shear strain in the shear band to range from ~10 (at 0.25 m/s) to ~40 (at 5 m/s). Shear strain rate in the shear band region was estimated to be ~4×10^5 s^{-1} at a cutting speed of 1 m/s.

Outeiro et al. [167] used the Digital Image Correlation (DIC) technique to estimate subsurface plastic strains produced in orthogonal cutting of OFHC copper at a cutting speed of 90 m/min. They estimated the maximum von Mises equivalent strain to be ~0.25 at 150 µm below the cut surface for an undeformed chip thickness (h) of 0.2 mm (Fig. 2). The authors note that further improvements in DIC are required to determine the maximum strains, which occur near the machined surface.

Accurate measurements of the cutting temperatures in the primary deformation zone, and in the secondary deformation zone, primarily due to tool-chip friction, are important for understanding their impact on the flow stress of the work material during cutting, and on the tool wear as well. High temperatures normally observed at the tool-chip interface accelerate tool wear, which can degrade the machined part surface integrity. However, the high temperatures in the secondary deformation zone normally do not affect work material behaviour in the primary deformation zone. As noted by Astakhov [11], under practical cutting conditions (Péclet number, Pe >> 10), the heat generated in the primary and secondary deformation zones is transported away from the zones by the fast moving chip because the chip velocity is much greater than the rate of heat conduction.

The challenge is to measure the temperatures in the primary deformation zone accurately and at a sufficiently high resolution.

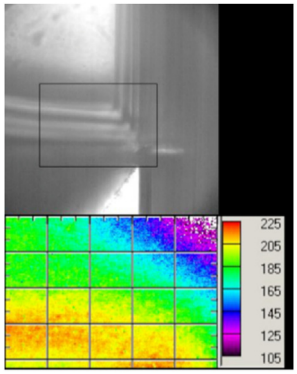

Fig. 4. Visible (top) and infrared temperature distribution in °C (bottom), obtained by high-speed videography of metal cutting (rectangle in visible image is ~0.3 mm horizontal infrared field of view) [117].

Davies et al. [65] presented a comprehensive review of cutting temperature measurement techniques. Choosing a reliable temperature measurement technique is a challenging task due to each method's measuring range limits, sensor capabilities (robustness, influence on process, signal type/sensitivity to noise, response time, and uncertainty), ease of calibration, cost, size, intrusiveness, etc. To address this issue, researchers at the National Institute of Standards and Technology (NIST) in the USA have developed special setups for high resolution and high speed temperature measurement by infrared thermography [117]. Fig. 4 shows an example temperature distribution in the primary deformation zone in orthogonal cutting of 7075-T651 Aluminium. It clearly shows that the peak temperature in the primary deformation zone barely exceeds 200 °C.

2.1.2. State of stress

According to Astakhov [13], metal cutting can be viewed as a forming process where the external energy applied to the cutting system causes separation of a layer of material from the bulk. Therefore, a principal difference between machining and all other metal forming processes is the physical separation of material in the form of a chip from the rest of the workpiece. The process of physical separation of a solid body into two or more parts involves fracture, and thus, machining must be treated as the purposeful fracture of the layer being removed. Significant work on this view of metal cutting has been reported by Atkins [14]. From this point of view, proper modelling of the work material in machining should take into account not only the material flow stress under the deformation conditions in machining, but also under conditions where fracture occurs [169]. Both flow stress and fracture are strongly dependent on the state of stress [27,169].

Classical metal plasticity theory assumes that only the second deviatoric stress invariant (J_2) influences the yield surface, as in the von Mises yield criterion. Thus, the hydrostatic stress (σ_m) has a negligible effect on strain hardening, and the flow stress is independent of the third deviatoric stress invariant (J_3) [27]. The hydrostatic stress is often expressed as a dimensionless quantity called the stress triaxiality parameter (η), defined in Eq. (1). The equivalent stress is often incorporated into the normalized Lode angle parameter ($\bar{\theta}$), defined in Eq. (2).

$$\eta = \frac{\sigma_m}{\bar{\sigma}} \tag{1}$$

$$\bar{\theta} = 1 - \frac{2}{\pi} arccos\left[\left(\frac{J_3}{\bar{\sigma}}\right)^3\right] \tag{2}$$

Recent experiments on plastic deformation of metals have shown that both the hydrostatic stress effect and the effect of the third deviatoric stress invariant should be included in the constitutive description of the material [27]. In general, the hydrostatic pressure controls the size of the yield surface while the Lode angle parameter is responsible for its shape. The effect of the Lode angle parameter on plastic yielding has been studied by Cazacu et al. [44] and Bacherla and Bassani [26]. These researchers proposed flow stress models that incorporate the difference in yield strength in compression and tension. However, their models do not have the flexibility to predict plane strain yielding. Such a generalization was proposed by Bai and Wierzbicki [27] who proposed a new form of an asymmetric metal plasticity model, considering the stress triaxiality (η) and Lode angle parameter ($\bar{\theta}$) effects. Recently, Buchkremer et al. [38] modified the Bai and Wierzbicki model to include strain-rate and temperature effects in the flow stress to simulate longitudinal turning of AISI 1045 steel.

Bai and Wierzbicki [27] also proposed a new fracture model that takes into account stress triaxiality (η) and the Lode angle parameter ($\bar{\theta}$). However, unlike the Johnson–Cook damage model [127], their fracture model does not account for the influence of strain-rate and temperature.

A key point of this discussion is that, to the extent possible, the role of stress state on plastic yielding and fracture of the metal should be accounted for in constitutive modelling. As discussed later, constitutive models for metal cutting routinely use flow stress data obtained under uniaxial loading conditions. This is because uniaxial loading experiments are easier to conduct than multiaxial loading experiments. However, the role of the state of stress and fracture in machining cannot be ignored.

2.2. Constitutive modelling

Constitutive models describe the relationship between stress and strain. The complexity of these relationships range from isotropic elastic models suitable for large-scale structural modelling, to crystal plasticity formulations designed to capture grain-scale inelastic behaviour. Prior knowledge of the deformation process is required for selection of an appropriate model.

As discussed previously, machining is unique in that the imposed deformations (strains, strain rates, temperatures, and state of stress) produce a complex thermomechanical loading history. Constitutive models may also be coupled with internal state variable (ISV) models that seek to capture the evolution of the underlying structure-related variables e.g., dislocation density, mean grain size, texture, etc. with deformation. The constitutive laws as well as ISV evolution equations may be described using phenomenological equations, physically-based equations, or some combination of the two.

2.2.1. Phenomenological models

Phenomenological constitutive models are commonly used to describe the high strain rate and high temperature flow stress response of metals in machining. These models are termed phenomenological because they describe material behaviour through empirically fitted functions of one or more macroscopic variables of deformation such as the plastic strain (ε_p), plastic strain rate ($\dot{\varepsilon}_p$), and temperature (T). The general form of such models is:

$$\sigma = \sigma(\varepsilon_p; \dot{\varepsilon}_p; T; \ldots) \tag{3}$$

The objective of this paper is not to review all phenomenological constitutive models in the literature but to critically discuss only those that are commonly used in machining simulations.

Table 1 summarizes the most frequently used phenomenological models used in cutting simulations. All of them assume isotropic deformation behaviour of the work material. Of the models listed in Table 1, the J–C model [126] is the most widely used because of its simplicity and relative ease of calibration. Its major drawback is that it is purely empirical and it is limited in its ability to accurately describe the constitutive behaviour of the material *outside* the range of the test data used to fit the model's parameters. As discussed by Leseur [140], the J–C model is unable to capture the increased strain rate sensitivity above 10^3 s^{-1}, often attributed to viscous drag based resistance to dislocation motion.

Table 1
Phenomenological constitutive models commonly used in metal cutting modelling and simulation.

Model	Pros and cons
Johnson–Cook (J–C) [126]: $\sigma = [A + B\varepsilon_p^n]\left[1 + C\frac{\dot{\varepsilon}^p}{\dot{\varepsilon}_0}\right]\left[1 - \left(\frac{T-T_0}{T_m-T_0}\right)^m\right]$	Pros J–C: Simple form with few parameters. Easy to calibrate. Pros modified J–C: Simple form with few parameters. Considers second order interactions. "tanh" term captures softening at large strains and temperatures, which allows shear banding to be simulated without a failure (damage) criterion. Cons J–C: Lacks explicit microstructural basis. Known to be inaccurate at high strain rates ($>10^3$–$10^4\,s^{-1}$). Does not intrinsically capture shear localization effects. Ignores second order interactions of strain, strain-rate, and temperature. Cons modified J–C: Lacks explicit microstructural basis. More involved model calibration procedure.
Modified J–C [41,211]: $\sigma = [A + B\varepsilon_p^n f(\varepsilon_p)][1 + C\frac{\dot{\varepsilon}^p}{\dot{\varepsilon}_0}]\left[1 - \left(\frac{T-T_0}{T_m-T_0}\right)^m\right]h(\varepsilon_p, T)$ $f(\varepsilon_p) = [exp(\varepsilon_p^a)]^{-1}, \quad h(\varepsilon_p, T) = [D + (1-D)tanh(\varepsilon_p + S)^{-c}]$ $D = 1 - \left(\frac{T}{T_m}\right)^d, \quad S = \left(\frac{T}{T_m}\right)^b$	
J–C: Empirical; Widely used. Modified J–C: Empirical.	
Strain Path Dependence Model [154,55]: $\sigma = A_1\left(\frac{\dot{\varepsilon}}{\dot{\varepsilon}_0}\right)^M e^{aT}\left(\frac{\dot{\varepsilon}}{\dot{\varepsilon}_0}\right)^m \left[\int_{strainpath} e^{-aT/N}\left(\frac{\dot{\varepsilon}}{\dot{\varepsilon}_0}\right)^{-m/N} d\varepsilon\right]^N$ $A_1 = f(T, \dot{\varepsilon})$	Pros: Models the strain path effect and its dependence on temperature and strain rate. Considers coupling of strain rate hardening and thermal softening. Cons: Requires incremental straining tests with simultaneous heating and quenching to capture strain path dependence. Lacks explicit microstructural basis.
Empirical. Well-developed for carbon steels and certain titanium alloys.	
Power Viscosity Law [156]: $\sigma = g(\varepsilon_p)\Gamma(\dot{\varepsilon}^p)\Theta(T)$ $g(\varepsilon_p) = \sigma_0\left[1 + \frac{\varepsilon_p}{\varepsilon_0}\right]^{\frac{1}{n}},$ $\Gamma(\dot{\varepsilon}^p) = \left[1 + \frac{\dot{\varepsilon}^p}{\dot{\varepsilon}_0}\right]^{\frac{1}{m}}; \Theta(T) = c_0 + c_1 T + \ldots$	Pros: Simple form with relatively few parameters. Easy to calibrate. Cons: Lacks explicit microstructural basis. Ignores second order interactions. Model parameter values in commercial software (e.g. Third Wave Systems AdvantEdge) inaccessible to user.
Empirical; Default model in AdvantEdge FEM software.	

σ : flow stress; ε_p : plastic strain; $\dot{\varepsilon}_p$:plastic strain rate; ε_0 : reference plastic strain; $\dot{\varepsilon}_0$: reference plastic strain rate; T: absolute temperature; T_0 : reference temperature; T_m : absolute melting temperature; *A, B, C, D, M, N, n, m, a, b, c, d*: empirically determined model parameters.

The original J–C model does not account for softening observed at the strains and temperatures in the primary shear zone, which is characteristic of metals that exhibit shear banding (e.g. Ti–6Al–4V). To address this limitation, Calamaz et al. [41] and Sima and Özel [211] modified the J–C model to accentuate the softening behaviour at large strains and temperatures, thereby enabling the simulation of shear banding without a material damage criterion.

Recently, a similar approach was used by Hor et al. [112] to model the constitutive behaviour of three steels for use in machining simulations. Although not physically-based, the modified J–C model has been shown to work well for simulating segmented chip formation in cutting of low thermal diffusivity metals such as titanium and nickel base alloys [219].

Umbrello et al. [221] modified the J–C model to include the effects of work material hardness in the flow stress. They used the model to predict the machined surface integrity in hard turning of AISI H13 and AISI 52100 steels.

Maekawa et al. [154] developed flow stress models that account for the strain path history dependence of flow stress. As discussed by Childs [49], variations of the model have been used successfully to simulate the machining response of carbon steels and titanium alloys.

There have been other attempts at incorporating the flow softening effect due to physical processes such as dynamic recrystallization. An example is the work of Rhim and Oh [187] who modified the J–C model using Avrami-type Arrhenius terms to simulate chip segmentation in cutting of AISI 1045 steel.

2.2.2. Physically-based models

The use of physically-based constitutive models in metal cutting modelling and simulation is a relatively recent development. In contrast to phenomenological models, physically-based constitutive models are based on microstructural aspects of plastic deformation. They mathematically describe the flow strength of a metal as a function of the microscale physical processes responsible for strengthening (e.g. dislocation-obstacle interaction) or softening (e.g. dynamic recovery, continuous dynamic recrystallization, grain boundary sliding) of the metal. It is well-known that during plastic deformation the microstructure continuously evolves as thermally activated mobile dislocations interact with short range and long range obstacles including the crystal lattice, solute atoms and precipitates, forest dislocations, and grain boundaries [158]. Strengthening or softening of the metal due to interaction of mobile dislocations with obstacles is governed by the strain, strain rate, and temperature. A general form of the physically-based constitutive model is [158]:

$$\sigma = \sigma(\rho_1, \rho_2; \dot{\varepsilon}_p, T) \tag{4}$$

$$\frac{d\rho_1}{d\varepsilon} = F_1(\rho_1, \rho_2; \dot{\varepsilon}_p, T) \tag{5}$$

$$\frac{d\rho_2}{d\varepsilon} = F_2(\rho_1, \rho_2; \dot{\varepsilon}_p, T) \tag{6}$$

where ρ_1 and ρ_2 represent microstructure parameters, e.g. average dislocation density and average grain size, respectively. Eq. (4)–(6) are mathematical descriptions of the evolution of the microstructure parameters with strain. It should be noted that these equations represent just one possible form of the physically-based constitutive model. For example, the flow stress could be dependent on other microstructure parameters, e.g. texture,

Table 2
Physically-based constitutive models used in metal cutting modelling and simulation.

Model	Pros and cons
Zerilli–Armstrong (Z–A) [232]: $\sigma = \sigma_a + Be^{-\beta T} + B_0\sqrt{\varepsilon_p}e^{-\alpha T}$ $\sigma_a = \sigma_G + k_d l^{-1/2},$ $\beta = \beta_0 - \beta_1 \ln\dot{\varepsilon}_p, \alpha = \alpha_0 - \alpha_1 \ln\dot{\varepsilon}_p$ General form of equation for bcc, fcc, and hcp metals. Limited use in machining.	Pros: Relatively simple form. Considers coupled strain rate and thermal effects on flow stress. Accounts for the initial microstructure of the metal. Considers relevant second order interactions. Cons: Must be modified for increased softening at large strains and high temperatures to simulate chip segmentation when not using a damage model.
Bammann–Chiesa–Johnson (BCJ) [103]: $\dot{\underline{\sigma}} = \lambda tr(\underline{D}^e)\underline{I} + 2\mu_l \underline{D}^e, \underline{D}^e = \underline{D} - \underline{D}^p$ Based on microstructure-property relationships. Uses internal state variables.	Pros: Accounts for hardening and recovery (static and dynamic) processes. Cons: Complex model with many material parameters. Microstructure parameters are not explicitly modelled. Extensive test data needed to fit the model parameters.
Mechanical Threshold Stress (MTS) Model [84]: $\sigma = \sigma_a + \sigma_{th}$ $\sigma_a = \alpha G b\sqrt{\rho},$ $\sigma_{th} = \sigma_0\left[1 - \left(\frac{kT}{g_0 G b^3}\ln\frac{\dot{\varepsilon}_0}{\dot{\varepsilon}}\right)^{1/q}\right]^{1/p}, \frac{d\sigma}{d\varepsilon} = \Theta_0 - \Theta_r(\dot{\varepsilon}^{T,\sigma})$ Based on thermal activation theory of plastic deformation.	Pros: Explicitly accounts for microstructure evolution with deformation and its impact on the flow stress. Can be adapted to include various micromechanical physics such as recovery and recrystallization, dislocation drag resistance at high rates, and grain boundary sliding. Cons: More involved parameter identification.

σ: flow stress; σ_G: athermal stress due to dislocation-grain boundary interaction; $\dot{\underline{\sigma}}$: time derivative of Cauchy stress tensor (rate form); σ_0: mechanical threshold stress (flow stress at 0 K); Θ_0: hardening (dislocation accumulation) rate; Θ_r: dynamic recovery rate; ε_p: plastic strain; $\dot{\varepsilon}_p$: plastic strain rate; ε_0: reference plastic strain; $\dot{\varepsilon}_0$: reference plastic strain rate; T: absolute temperature; $\underline{D}$: total deformation tensor; $\underline{D}^e$: elastic deformation tensor; $\underline{D}^p$: plastic deformation tensor; λ, μ_l: Lame' constants; G: shear modulus; b: magnitude of Burger's vector; ρ: dislocation density; l: average grain size; k: Boltzmann's constant; g_0: normalized activation energy at 0 K; B, B_0, β_0, β_1, α_0, α_1, α, k_d, k, p, q: model calibration parameters.

whose evolution with deformation would then have to be modelled.

Due to their complexity, physically-based constitutive models have seen limited use in metal cutting modelling and simulation. Nevertheless, they are an important advancement since they intrinsically permit the simulation of microstructure and mechanical properties (e.g. hardness [145], residual stress [66]) of the machined surface, and, in addition, they can more accurately describe the material response to loading outside the model calibration range.

Examples of physically-based constitutive models used in metal cutting modelling and simulation are given in Table 2.

The Zerilli–Armstrong (Z–A) constitutive equations are motivated by the well-known theory of thermal activation of dislocations [233]. They model the flow stress as a summation of athermal and thermal stress terms that are functions of the strain, strain rate, and temperature. Differences in the flow stress behaviours of fcc, bcc, and hcp metals are captured by the equations, which account for the coupling of strain hardening, strain rate hardening, and thermal softening, as appropriate for the crystal structure of the metal under consideration [233,232].

The Z–A models have seen limited use in metal cutting. Jaspers and Dautzenberg [121] used the Z–A equations to model the flow stress of AISI 1045 steel (bcc) and AA6082-T6 (fcc) and found that while the model for AISI 1045 steel described the flow stress well, the fcc equation for AA6082-T6 did not fit the flow stress data very well. Childs and Rahmad [56] showed that the bcc Z–A model, when modified to include an upper yield point at low strains ($<$0.05) typical of carbon steels, produced slightly better results than a power law model for simulating the plane strain cutting of carbon steels. In later work, they [57] showed that acceptable values of forces, shear angle, and shear stress could be obtained through a simpler, albeit heuristic, modification of the strain hardening exponent. Liu et al. [143] modified the hcp Z–A model to account for increased softening, which was attributed to dynamic recovery and recrystallization at large strains and temperatures, to simulate chip segmentation in orthogonal cutting of Ti–6Al–4V.

Guo et al. [103] used the ISV based Bammann–Chiesa–Johnson (BCJ) model to simulate metal cutting. Although the BCJ model incorporates the effects of several physical processes active during plastic deformation, it is complex and requires a large amount of carefully controlled test data to fit the 18 model parameters. This makes the model difficult to establish and therefore less practical.

Svoboda et al. [214] used the Mechanical Threshold Stress (MTS) model to simulate orthogonal cutting of 316L stainless steel. They used dislocation density and vacancy concentration as ISVs to describe the evolution of microstructure with plastic deformation. Their model is the first documented instance of a microstructure dependent physically-based constitutive model used in metal cutting simulation. In later work, Wedberg et al. [224] extended Svoboda et al.'s model to include the effect of dislocation drag on the flow stress at high strain rates. While their finite element (FE) simulation of orthogonal cutting of 316L stainless steel yielded good results for forces and chip thickness, it is not clear if their models can simulate chip segmentation, which is known to occur in stainless steels.

Recently, Liu et al. developed a MTS based ISV model for simulating continuous chip formation in OFHC copper [146] and segmented chip formation in pure titanium [159]. In their model, the flow stress is a function of microstructure, which is described by the evolution of the dislocation density and the mean grain size. The effects of dislocation drag, dynamic recovery, and dynamic recrystallization are also considered. Below a critical grain size, an inverse Hall-Petch effect, attributed to grain boundary sliding, is included in the model to simulate segmented chip formation [159]. Fig. 5 shows the model's ability to simulate severe grain refinement in the shear band region of the chip. The model has a large number of parameters whose identification is non-trivial.

Ding and Shin [68] used Estrin et al.'s [74] unified model of plasticity to describe the flow stress as a function of dislocation density evolution. In their model, dislocation density is the sole microstructure parameter. The grain size is assumed to equal the evolved dislocation cell size, which is inversely proportional to the square root of the total dislocation density. Ding and Shin showed their model was able to accurately simulate the cutting force and strain evolution in the primary shear zone in orthogonal cutting of pure titanium [69], albeit at very low cutting speeds where shear bands do not form. It is unclear however if their constitutive model

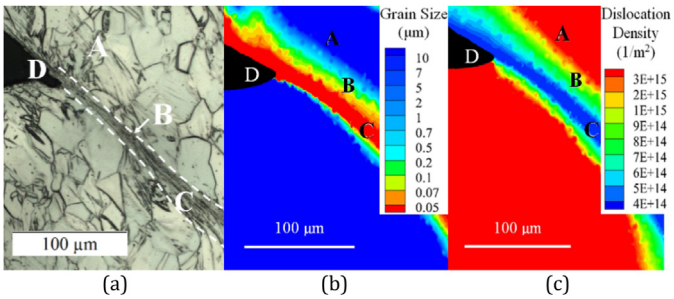

Fig. 5. (a) Optical micrograph of chip microstructure in the shear band, and simulated (b) grain size and (c) dislocation density distribution (cutting speed = 100 m/min, uncut chip thickness = 0.2 mm) [159].

is capable of simulating shear localization seen in many metals including pure titanium, especially at higher cutting speeds.

Atmani et al. [17] used the original MTS model with Estrin et al.'s [74] microstructure evolution model to simulate grain refinement in orthogonal cutting of OFHC copper. Their model shows good agreement with experimental data. Denguir et al. [66] integrated the effects of the state of stress and dynamic recrystallization in the J–C model to simulate the machined surface integrity in orthogonal cutting of OFHC copper.

It is clear from the preceding discussion that researchers are trying to develop increasingly complex physically-based constitutive models for machining simulation. It is anticipated that this trend will continue in the near future, and will be driven by the metal machining needs of the industrial sector.

2.3. Experimental techniques for determining the mechanical behaviour of metals in cutting

Development and calibration of constitutive models for metal cutting requires representative experimental data. During metal cutting, the deformation history of the work material is complex and ranges from room temperature and quasi-static conditions ahead of the deformation zone to high temperatures and dynamic rates in the primary and secondary deformation zones. Additionally, the state of stress in metal cutting is always multiaxial with a wide range of stress triaxiality and Lode angles. Therefore, the experimental techniques used to determine the mechanical behaviour of metals should be able to accurately reproduce the strains, strain rates, temperatures, and states of stress in metal cutting.

2.3.1. Quasi-static and dynamic tests

Conventional cross-head devices such servo-hydraulic or screw-driven test frames are capable of performing uniaxial and multi-axial experiments to large strains in the quasi-static regime (10^{-5}–10^{0} s^{-1}). Elevated temperatures can be achieved when coupled with induction or furnace heating. Thermal–mechanical simulators (Gleeble systems) can be used to perform large strain uniaxial compression tests at elevated temperatures and strain rates up to 10^{1}–10^{2} s^{-1} (Fig. 6). However, the strain rates produced in these tests

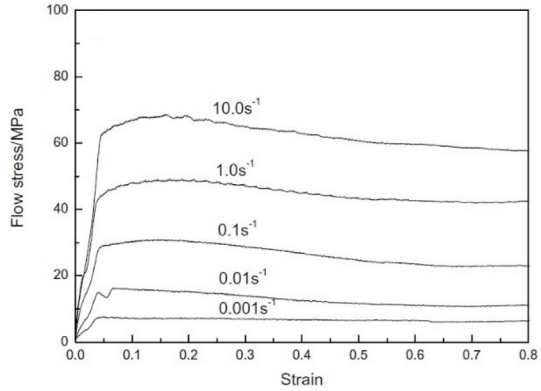

Fig. 6. Ti–6Al–4V flow stress curves at 1303 K produced using the Thermecmaster-Z thermal-mechanical simulator [149].

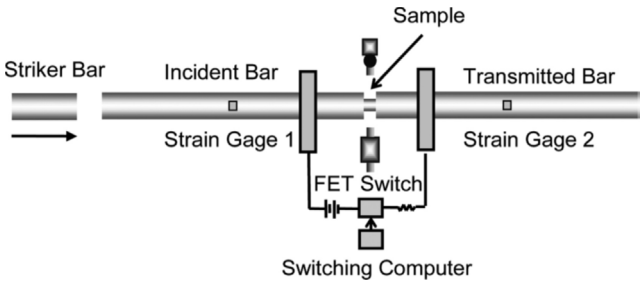

Fig. 7. Schematic of the NIST electrical pulse-heated Kolsky bar setup [39].

are usually lower than those produced in metal cutting. Therefore, dynamic or impact testing techniques are needed.

The most common dynamic material testing technique is the Split-Hopkinson Pressure Bar (SHPB), also referred to as a Kolsky bar [131], which can generate strain rates on the order of 10^{3}–10^{4} s^{-1}. Variants of the original SHPB technique allow for tensile and torsion loadings [163]. Depending on the material, the strains imposed in these experiments are usually much less than 1. However, repetitive testing on a single sample can be used to impose larger accumulated strains. The use of a hat-shaped specimen permits the study of shear banding at large strains [4]. Such specimens have been used to study the susceptibility of various alloys to adiabatic shear band failure [160].

According to Burns et al. [39], the traditional elevated temperature Kolsky bar does not account for the combination of high heating rates (>1000 °C/s) and high loading rates (~10^{4}/s) seen in machining. Using an electrical pulse-heated Kolsky bar setup (Fig. 7), they showed that the flow stress of a rapidly heated near-eutectoid steel decreased by 50% due to time-dependent thermally-activated microstructure evolution, which is not captured by the standard J–C constitutive model.

Achieving higher strain rates (10^{6}–10^{8} s^{-1}) than normally possible with a SHPB apparatus requires shock inducing impact tests [79]. These tests are multiaxial in nature and therefore the flow stress curves cannot be directly inferred. One popular high-rate testing technique is the rod-on-rigid-anvil or Taylor impact experiment, where a projectile is launched at a rigid boundary, which produces a deformed sample. Even though flow stress curves cannot be extracted from these tests, constitutive models can be "tuned" to match the shape of the deformed sample, as shown in Fig. 8. However, till date, such testing methods have not

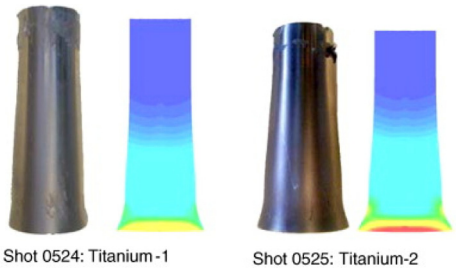

Fig. 8. Experimental and simulated hcp titanium samples obtained in reverse anvil-on-rod impact tests [157].

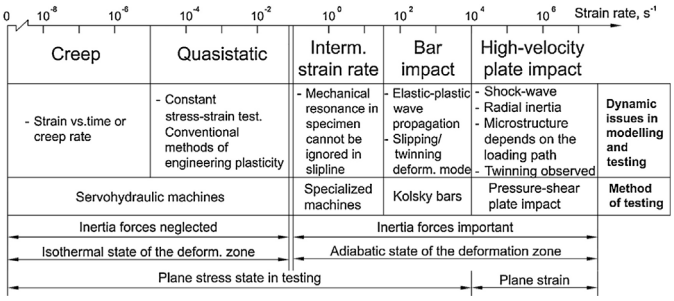

Fig. 9. Experimental techniques for different strain rate regimes (adapted from [137]).

been utilized by the machining research community. Other high rate tests include ballistic penetration tests and plate impact tests [137]. A summary of the major testing regimes and the associated materials test methods is given in Fig. 9.

2.4. Identification of constitutive model parameters

The choice of a constitutive model is extremely important to accurately describe the mechanical behaviour of the work material. Equally important is the identification of constitutive model parameters. These parameters are usually identified from experimental data obtained from mechanical [111] and/or machining tests [172]. Different methods, including direct and inverse methods, can be used to identify the model parameters [28].

The direct method consists of explicitly determining the constitutive model parameters as a function of the model variables. This method can be applied to simple constitutive models with few parameters (e.g., the power law). For complex constitutive models with many parameters, the inverse method, which utilizes optimization-based approaches, is the best solution for identifying the model parameters. The inverse method consists of simulating the experimental test by modifying the constitutive model parameters iteratively to minimize the difference between the predicted and measured data [28]. Several optimization-based methods (see Table 3) can be used for this purpose [45,222].

The derivative-free search and gradient-based algorithms are relatively simple to use but they depend strongly on the initial guess and tend to converge to the local minima. However, derivative-free search methods are simpler to use than gradient-based methods since they don't need to compute derivatives. Both algorithms are strongly dependent on user skills. Germain et al. [85] used the Levenberg–Marquardt algorithm to identify the optimal J–C model parameters for two titanium alloys using data from compression tests at high strain-rates and temperatures.

Evolutionary algorithms such as Genetic Algorithms (GA) and Particle Swarm Optimization (PSO) are more robust than other algorithms since they use mechanisms to improve the initial solution and, in general, do not converge to the local minima. However, they are computationally expensive and convergence to the global minimum is not always guaranteed. Özel and Karpat [171] used a cooperative PSO algorithm on SHPB test data to identify the J–C model coefficients for several work materials.

Hybrid approaches that combine the advantages of two or more algorithms, such as the robustness of evolutionary algorithms and the performance of gradient-based algorithms, can also be used. Chaparro et al. [45] used both gradient-based and evolutionary algorithms to identify the constitutive model parameters for an Aluminium alloy using flow stress data obtained from tension tests, and data from monotonic and Bauschinger shear tests.

Depending on user skills and methods used to identify the model parameters, the results obtained from these algorithms can vary greatly. This contributes to the inconsistencies often observed in the model parameters reported in literature [45].

Table 3
Optimisation-based methods.

Method	Algorithm
Gradient-based	Steepest descent
	Newton and quasi-Newton
	Levenberg–Marquardt
	Sequential quadratic programming
	Globally convergent method of moving asymptotes
Derivative-free search	Pattern search
	Rosenbrock
	Simplex
	Powell
Evolutionary algorithms	Genetic algorithms
	Particle swarm optimization
	Simulated annealing

2.5. Critical assessment of material behaviour and constitutive models

The accuracy of constitutive models and associated data for metal cutting simulations depends greatly on [107,49]: (i) the materials testing technique and the thermo-mechanical loading conditions utilized to obtain the flow stress data used to fit the model parameters, (ii) the model chosen and the physics therein, especially when extrapolating the model outside its calibration range, (iii) prior processing history and microstructure of the material used to generate the flow stress data, and (iv) the model parameter identification algorithm employed.

It is commonplace for machining researchers to fit constitutive models to high strain rate data obtained from uniaxial SHPB compression tests performed over a range of temperatures. As pointed out by Childs [49], such models yield acceptable shear stress values for the primary shear zone where the strains and temperatures are generally lower than at the tool-chip interface. However, the flow stress corresponding to temperatures at the tool-chip interface tends to be overestimated by the model due to the inability of standard dynamic material tests to faithfully reproduce the higher strains and temperatures seen in the secondary shear zone.

The dependence of the accuracy of machining simulations on the test method and the associated loading conditions can be seen from the work of Hor et al. [112], where a J–C model fitted with dynamic shear test data yielded peak temperatures closer to the experimental value than a model fitted with dynamic compression data. Even though the stress state in metal cutting is multiaxial, acceptable predictions (<10–15% error) of the forces, shear angle, and deformed chip thickness can be obtained from constitutive equations fit to uniaxial flow stress data (mostly from quasi-static and/or dynamic compression tests). Hor et al.'s [112] results also suggest that the primary deformation mode (compression vs. shear) in the materials test may be important for accurate prediction of quantities such as temperatures, strains, etc.

The choice of a constitutive model can impact the accuracy of machining simulations, as discussed by a number of authors [41,211,112,103,121,209,81,52,1]. Fig. 10 shows a comparison of flow stress curves and machining simulations using two constitutive models for OFHC copper.

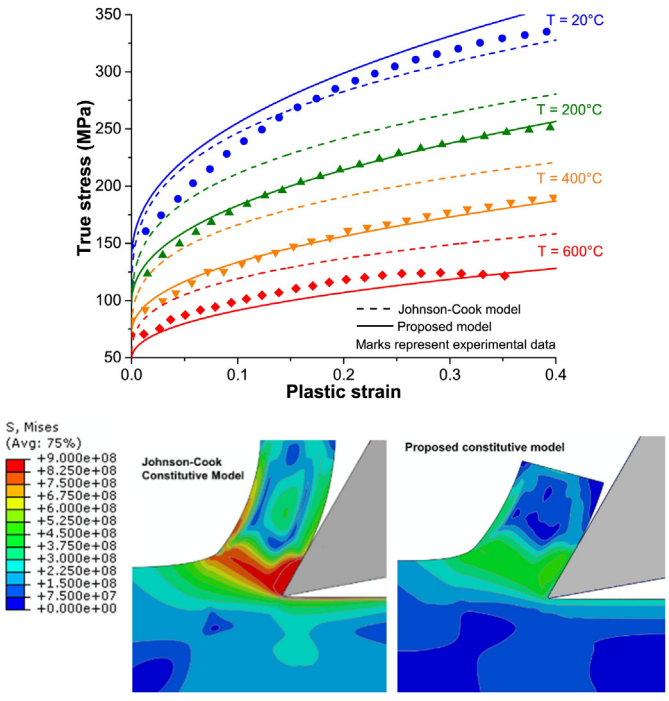

Fig. 10. Influence of constitutive model on the flow stress and machining simulations for OFHC copper [66].

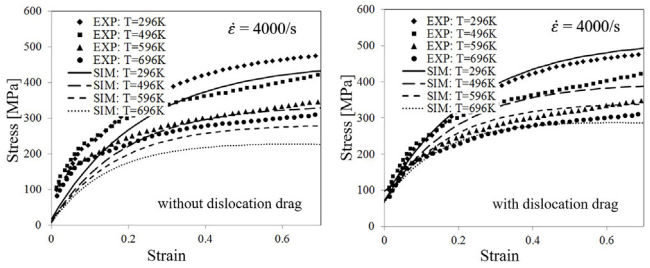

Fig. 11. Effect of dislocation drag physics in MTS-type constitutive model for OFHC copper [146].

The deformation physics contained in the model also impacts the simulation accuracy. This can be seen in Fig. 11 where an MTS-type model for OFHC copper with and without dislocation drag is compared against experimental data. The work of Childs and Rahmad [56] also highlights the importance of including the correct deformation physics in the constitutive model to ensure the accuracy of cutting simulations. In the absence of a damage evolution model, Melkote et al. [159] showed that an inverse Hall-Petch effect must be included in the constitutive model to capture shear bands formed in the cutting of pure titanium. This need is supported by evidence of severe grain refinement in titanium chips [205].

Researchers in the machining community routinely use flow stress data from literature to fit constitutive models. Often, the processing history and microstructure of the material used to generate the flow stress data are unknown, leading to potentially significant differences between the microstructures of the materials used to generate the flow stress and the cutting data, respectively. This can lead to erroneous constitutive modelling and inaccurate cutting simulations. For example, it is well-known that the heat treatment process routes greatly influence the bulk microstructure and its deformation response. This is especially true of Ti–6Al–4V, Ni-based super alloys, and steels. Fig. 12 illustrates the dependence of flow stress of Ti–6Al–4V on the initial microstructure. It is therefore imperative for researchers to ensure consistency in the initial microstructures when using data from literature and to report the prior heat treatment and initial microstructure of the work material.

Since chip formation in metal cutting involves physical separation of the material from the bulk, proper constitutive modelling should account for not only the material flow stress under machining conditions, but also for a physically-meaningful damage model or criterion for material separation (fracture) [169].

The method for constitutive model parameter identification can yield non-unique model parameters for a given material. It is not uncommon to find reports of different model parameter values for the same material. Reasons for the non-uniqueness of the model parameters include the nonlinear optimization method used to determine their values [172], the type of flow stress data used to fit the model (e.g. compression vs. shear) [112,111], and the ranges of strains, strain rates, and temperatures produced in the flow stress determination tests. For a given constitutive model, a detailed sensitivity analysis and validation against experimental data, similar to that reported by Childs [51], is necessary to identify the model parameter values that yield physically meaningful results.

In summary, constitutive model development for metal cutting modelling and simulation continues to be an active research area. While the major focus of recent work is on developing physically-based constitutive models, the use of simpler models (e.g., J–C) is very common. This is due to the ready availability of model parameter values for common engineering metals such as carbon steels, aluminium alloys, and certain super alloys (e.g. Ti–6Al–4V), as well as the ease of parameter identification for such models.

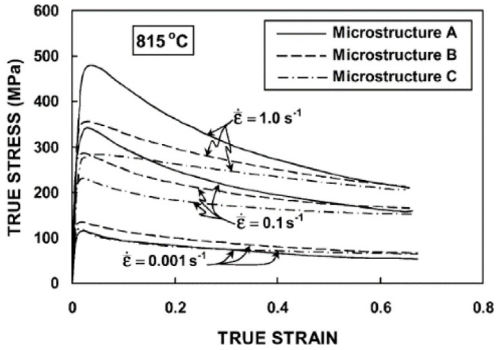

Fig. 12. Flow stress curves for three distinct Ti–6Al–4V microstructures obtained from different heat treatments [201].

2.6. Future needs and opportunities

1. A systematic and detailed comparison of the relative performance of different constitutive models in simulating the metal cutting process.
2. Knowledge of which constitutive model—phenomenological or physically based—to use for a given engineering alloy over the range of economic cutting conditions for the alloy. A database of validated flow stress models for common engineering alloys could be created by CIRP and made available to industry practitioners and the academic research community.
3. Development of a materials testing technique that is economical and is capable of capturing the ranges of strains, strain rates, temperatures, and the state of stress routinely seen in metal cutting.
4. Better understanding of the effects of heat treatment and starting microstructures on the material flow stress.
5. Development of material damage (fracture) models that are applicable to metal cutting.

3. Friction data and models

3.1. Tribological phenomena at the tool-work material interface

3.1.1. Friction in metal cutting process

Friction between contacting bodies is important in all engineering applications where solid metallic surfaces are in sliding contact with each other. This is particularly important in metal cutting where the plastic deformation of the softer counterpart (work material) takes place under high normal pressure. The size of contact (contact length) is determined by the cutting behaviour, and contact takes place on both the rake and flank faces depending on the cutting conditions. Energy is dissipated during relative motion of the contacting surfaces of the tool, the chip, and the freshly formed machined surface. In addition, friction is influenced by tool wear, which increases energy consumption. The dimensionless friction quantity is the coefficient of friction, defined as the ratio of forces acting parallel (F) and perpendicular (N) to the interface between the two bodies in relative motion (μ=F/N).

In general, three generic physical mechanisms are responsible for friction (Fig. 13), namely [110]:

- Adhesion (μ_a), which involves the shearing of micro-welded junctions formed by contacting surface asperities at high pressure and temperature.

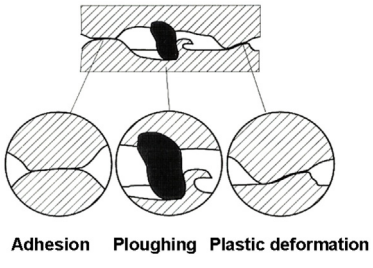

Fig. 13. Three basic components of sliding friction [110].

- Plastic deformation of asperities (μ_d), causing material flow when a body slides over another, which is responsible for the static coefficient of friction.
- Ploughing action of rounded cutting edges (μ_p), which produces a groove due to plastic flow but without removing material.

The dominant mechanism of sliding friction tends to be the adhesive interaction between the surface asperities, especially for non-viscoelastic materials. However, rougher contacting surfaces and tool wear result in more intense plastic deformation of asperities, which increases the friction.

Adhesion and plastic deformation as the dominant frictional phenomena are integrated in a molecular-mechanical theory of friction developed by Kragelsky et al. [136]. This friction concept was used to predict the roughness height [90]. The presence of the three basic friction mechanisms was confirmed in a macroscopic concept of friction, called the genesis of friction [213]. The following typical values of the three components of the coefficient of friction were experimentally determined (maximum values in brackets): μ_a = 0–0.4(0.51), μ_d = 0–0.43(0.75), and μ_p = 0–0.4(1.0).

Accordingly, an important mechanism of friction is ploughing of the contacting surfaces by the hard asperities and wear particles. However, its participation depends on the tribological contact conditions. The presence of low-friction coatings and fluid lubricants drastically reduces friction.

Friction modelling is a very difficult task due to a number of potential influencing factors including the contact microgeometry (surface roughness), relative motion (constancy of motion, surface velocity), applied forces (contact pressure, constancy of applied forces), temperature (thermal effects on the material and lubricant properties), and stiffness and vibration (contact compliance, damping of frictional vibrations, feedback between frictional stimulus and structural response).

In general, the values of the coefficient of friction used in analytical and numerical modelling of metal cutting are much lower than those measured in orthogonal cutting tests. The models assume μ = 0–0.5(0.6), whereas experimentally obtained values can exceed 1 and sometimes approach 2(3) [12].

3.1.2. Concept of friction at the macroscopic scale

Under highly loaded conditions at the chip-tool contact, there is a region of complete plastic contact, which restricts lubrication by fluids or gases during continuous chip formation. The friction stress between the chip and tool is equal to the shear yield stress of the chip at the prevalent strain, strain-rate, and temperature. Lubrication typically reduces the tool-chip contact length. Within the reduced contact length, the friction stress is higher than under normal contact conditions. However, solid lubrication is possible in the case of a free-machining metal [55,50].

In interrupted cutting, such as in milling, there can be an initial period of lubricated cutting during which pre-existing lubricant films are worn away. This was explored in the context of Minimum Quantity Lubrication (MQL) in Ref. [116].

$$\tau = \min.(\mu\sigma_n, \overline{\sigma}/\sqrt{3}) \tag{7}$$

Eq. (7) is a well-known friction law. The friction stress τ is the lower of $\mu\sigma_n$ and $\overline{\sigma}/\sqrt{3}$ where μ is the friction coefficient, σ_n is the normal stress between the chip and the tool, and $\overline{\sigma}$ is the equivalent flow stress of the chip material (for a free-machining material, $\overline{\sigma}/\sqrt{3}$ may be corrected by a factor $m < 1$). This law recognises the changing contact conditions at the chip-tool interface as the distance from the cutting edge increases, from $\tau = \overline{\sigma}/\sqrt{3}$ near the cutting edge to $\tau = \mu\sigma_n$ towards the end of contact. In FE simulations of dry machining of a series of carbon and low alloy steels, good agreement with experimental results was obtained by assuming a friction coefficient greater than 1.0 [57]. This is in agreement with the results presented in Refs. [55,50,48]. The assumption is also applicable to the micro-machining of steel and built-up-edge formation in the cutting of steel [53].

An improved friction mechanism that integrates the effects of adhesion and ploughing can be derived from a slip-line field analysis of the contact between a rigid-plastic plane and a rigid wedge-shaped asperity [134]. The sliding of a hard metal surface over a soft surface is assumed to result from the pushing of waves of plastically deformed material in the soft surface ahead of the asperities on the hard surface.

3.2. Friction models

3.2.1. Review of existing tool-chip interface friction models

Realistic characterization of the frictional interaction between the chip and the tool is necessary to model the behaviour of the secondary deformation zone.

In the past, and in current practice, the tool rake face friction has been modelled in terms of a constant coefficient of friction based on the Coulomb friction model.

The average coefficient of friction at the tool-chip interface can be calculated from the cutting forces or from the average tool-chip contact stresses (see Fig. 14) [92]. The relationship between the friction force F_γ and the normal force $F_{\gamma N}$ yields an average friction coefficient at the rake face as follows:

$$\mu_\gamma = \frac{F_\gamma}{F_{\gamma N}} = \frac{F_c \sin\gamma_0 + F_f \cos\gamma_0}{F_c \cos\gamma_0 - F_f \sin\gamma_0} \tag{8}$$

where F_c is the cutting force, F_f is the feed force, and γ_0 is the orthogonal rake angle.

The model linking the average shear ($\overline{\tau}_f$) and normal stresses ($\overline{\sigma}_n$) acting on the rake face is given by:

$$\mu_c = \frac{\tau_t A_p}{\sigma_t A_p} = \frac{\overline{\tau}_f}{\overline{\sigma}_n} \tag{9}$$

where A_p is the apparent area of contact, τ_t and σ_t are the shear strength and yield stress of the softer (chip) material.

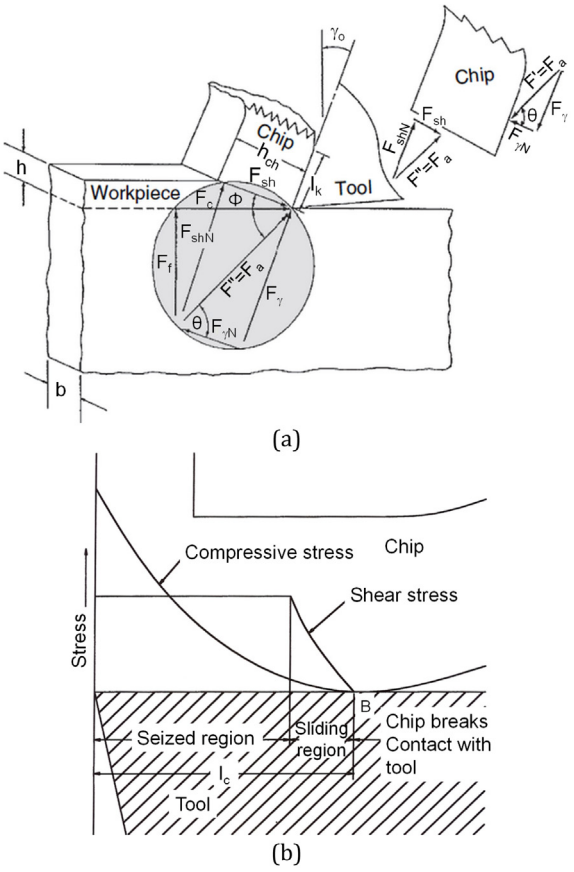

Fig. 14. (a) Merchant's shear plane model of forces in the chip formation zone, and (b) Zorev's contact stress distribution model [92].

Zorev's sticking-sliding model shown in Fig. 14b distinguishes the zone of sticking (seizure or plastic contact) near the tool edge and sliding (elastic contact) beyond the sticking region. The compressive normal stress is maximum at the cutting edge and falls to zero at the end of tool-chip contact. The shear stress exhibits a plateau in the sticking zone and decreases in the sliding zone. The distribution of normal stresses is given by:

$$\sigma_c = \sigma_{c\max}(x/l_c)^n \tag{10}$$

where l_c is the tool-chip contact length, x is the distance from the chip separation point, and n is an exponent parameter.

In the sliding zone, the stress distribution satisfies the Coulomb friction law as follows:

$$\tau_c = \mu\sigma_c \tag{11}$$

In the sliding region, the ratio of the real contact area A_r to the apparent contact area A_p is very small and the Coulomb–Amonton law describes the friction behaviour. In contrast, in the sticking region A_r/A_p continuously increases and, in the vicinity of the cutting edge, it approaches 1. This means that the coefficient of friction reaches the theoretical maximum of 0.577, which satisfies the von Mises plastic flow rule.

The maximum value of the friction coefficient can also be determined by [92]:

$$\mu_{c\max} = 1/[2(1.3 \pm \gamma_0)] \tag{12}$$

where γ_0 is the orthogonal rake angle measured in radians.

For constant shear friction along the entire tool-chip interface, friction is determined using a shear friction factor m as follows:

$$\tau = mk \tag{13}$$

where k is the shear flow strength of the work material at the tool-chip interface. Typically, m ranges from 0.1 to 0.8(0.9) [80]. For $m = 1$, plastic contact (seizure) occurs.

Shirakashi and Usui [210] derived a friction stress equation as follows:

$$\tau_f = k(1 - e^{-\mu\sigma_n/k}) \tag{14a}$$

where τ_f and σ_n are the friction and normal stresses, respectively.

In Eq. (14a) the friction and normal stresses are fitted to data from a split tool experiment for α-brass, pure aluminium, and S15C low carbon steel. The equation reduces to Eq. (11) at low values of σ_n and saturates at the shear flow stress k at high values of σ_n.

Further modification of Eq. (14a) concerns the transition between $\tau_f = \mu\sigma_n$ and mk due to the fact that for free-cutting steels the saturation value is not k but mk. By multiplying k with a friction factor m, where $0 < m < 1$, a modified equation is obtained:

$$\tau_f = mk(1 - e^{-\mu\sigma_n/mk}) \tag{14b}$$

Alternatively, the limiting friction stress at a point in the chip-tool contact can be replaced by $\overline{\sigma}/\sqrt{3}$, where $\overline{\sigma}$ is the equivalent flow stress [50], yielding the following equation:

$$\tau_f = \frac{\overline{\sigma}}{\sqrt{3}}\left(1 - e^{(-\mu\sigma_n\sqrt{3}/\overline{\sigma})}\right) \tag{15}$$

A further improvement of the friction model is to replace a constant friction coefficient by one that increases with the effective plastic strain:

$$\mu = \mu_0(1 + \overline{\varepsilon}_p) \tag{16}$$

Taking into consideration the fact that in cutting a newly created surface directly contacts the tool face, Iwata et al. [118] proposed the following empirical equation:

$$\tau_f = \left(\frac{H_v}{0.07}\right) \tanh\left(\frac{0.07\mu p}{H_v}\right) MPa \tag{17}$$

where H_v is the Vickers hardness of the workpiece material, and p is the contact pressure in MPa.

In the molecular-mechanical theory of friction, the total coefficient of friction consists of the adhesion and mechanical components as follows [136,90]:

$$\mu = \mu_a + \mu_m \tag{18}$$

The friction components μ_a and μ_m are derived in Ref. [90]. Another model with a transition zone was proposed recently by Zhou [236].

The coefficient of friction for the wave contact model proposed by Kopalinsky and Oxley is given by [134]:

$$\mu = \frac{A \sin\alpha + \cos(\arccos f - \alpha)}{A \cos\alpha + \sin(\arccos f - \alpha)} \tag{19}$$

where $A = 1 + \frac{\pi}{2} + arc\cos f - 2\alpha - 2.\arcsin[(1-f)^{-1/2}\sin\alpha]$, f is the normalized film strength given by $f = \tau/k$, τ is the shear strength of the film, k is the shear flow stress of the deforming material, and α is a surface roughness parameter. For $0 \le f < 1$, μ lies in the range $0 \le \mu < 1$. For full adhesion, μ is close to 1. On the other hand, for a small residual ploughing component of friction, $\mu = \cot\alpha$ [115]. The asperity deformation model has been found to be in good agreement with experimental results.

3.2.2. Comparative assessment of existing friction models

The distribution of the normal and shear stresses on the rake face of a cutting tool, shown schematically in Fig. 14b, has been verified to determine the real pattern of stress changes along the tool's rake and flank faces. In these experiments, the stress distribution at or very near the cutting edge, obtained from a split tool and photoelasticity technique, is not very accurate.

Fig. 15 shows several examples of the tool rake face stress distributions obtained for different materials using the split tool technique. The contact stresses are normalized by the shear flow strength k, and the distance from the cutting edge is normalized by the chip thickness. In most cases, the normal stress rises to a peak near the cutting edge and ranges from 0.7 k to 2.5 k. However, for nonferrous metals such as aluminium and copper, the normal stress tends to a visible plateau.

In general, during metal cutting, the mean coefficient of friction is substantially affected by the cutting speed (partly due to thermal softening), the feed rate (via the normal load), the rake angle (by controlling the intensity of plastic deformation in the primary deformation zone), and by modification of the tribological conditions through low-friction coatings [92]. For AISI 1045 and AISI 304 steels and a number of single and multilayer tool coatings,

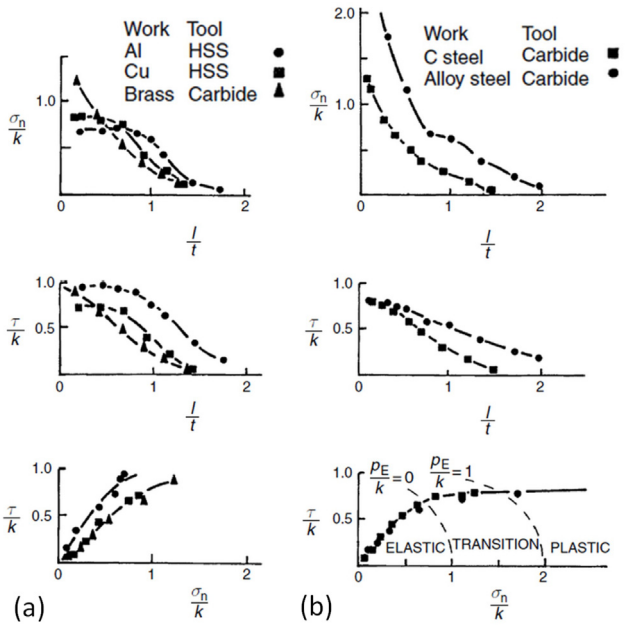

Fig. 15. Experimentally determined contact stresses for (a) non-ferrous, and (b) ferrous metals, using the split tool technique [92].

it has been shown that the reduction in contact area and thermal softening of the workpiece influence the contact stresses and the frictional behaviour [12,99].

3.3. Experimental methods for determining the friction data for machining

Determination of the friction coefficient in machining can be realized by at least three different methods:

- cutting force measurements,
- conventional tribometer,
- special tribometer designed for cutting applications.

The first approach is usually based on the turning [172,50,99,95] or the milling process [197]. The cutting forces, chip dimensions, and the tool-chip contact surface are measured and analysed. However, the friction coefficient varies along the contact [184,212] due to variation of the local sliding velocity, contact pressure, and temperature. Consequently, this approach is unable to distinguish between the sticking and sliding zones of contact. In order to overcome this problem, authors use either a split tool or analytical models. A proposal to improve this method by combining interrupted turning with in-depth analysis of the secondary deformation zone has been presented [151].

The second approach for determining the friction coefficient uses conventional tribometers without surface refreshment and is independent of any cutting process. The most common tribometer is the pin-on-disc, which is easy to use. The disc is made of the work material while the pin is made from the cutting tool material. This approach has been used by several researchers [199]. Commercial cutting tool inserts may also be used instead of pins. Unfortunately, such tribometers do not simulate the relevant tribological conditions at the tool-work interface in cutting. However, it has been documented [199,35] that such friction data can aid in improving the accuracy of numerical simulations of cutting.

The third approach involves the use of special tribometers (Fig. 16) that simulate open tribological conditions with different sliding velocities and contact pressures. A popular configuration (Fig. 16b) uses a pin placed just after a cutting tool during the machining of a tube face [166]. In this case, the pin rubs against a continuously refreshed surface and the sliding speeds and contact temperatures replicate dry machining. However, the contact pressures in this method are only around 15 MPa whereas the contact pressures in cutting are on the order of a few GPa. Several devices [212,229] have been developed to increase the contact pressure under high sliding velocities or to investigate the effects of lubrication.

The experimental set-up shown in Fig. 16f is similar to orthogonal cutting of a disc using a real cutting tool with an extremely negative rake angle [180]. However, during a single rotation of the workpiece and the very short contact time, it is difficult to achieve a steady thermal state. This method was further refined by using a broaching machine [181].

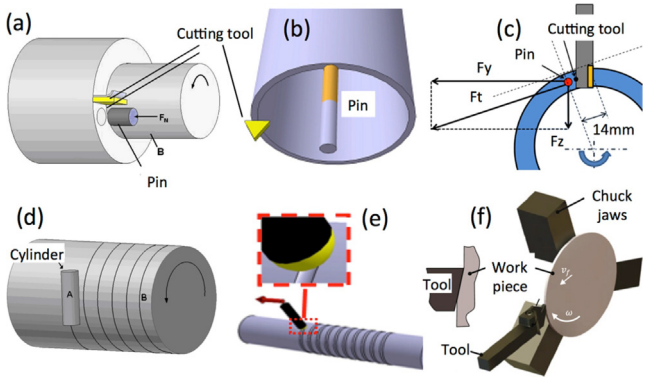

Fig. 16. Open tribometers for determining friction in cutting. Designed by (a) Olsson et al. [166], (b) Zemzemi et al. [229], (c) Smolenicki et al. [212], (d) Hedenqvist and Olsson [108], (e) Claudin et al. [60], (f) Puls et al. [180].

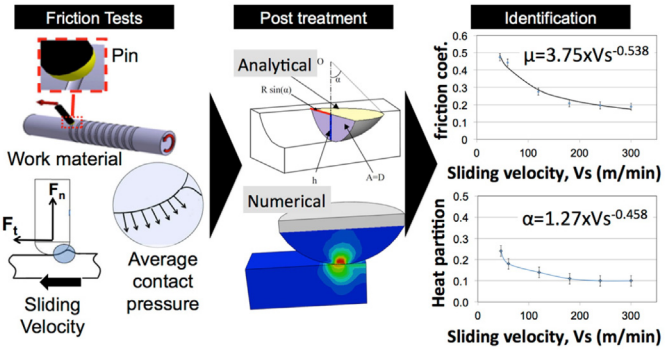

Fig. 17. Procedure to identify friction models from laboratory tests as proposed by Zemzemi et al. [229].

As an alternative, an open tribometer simulating the contact conditions in cutting over a longer time scale (Fig. 16e) was proposed [60]. A cylindrical pin rubs on a fresh surface during rotation and the surface refreshment is discontinuous. A large feed of the pin enables a helical movement in order to avoid superposition of the scratches produced on the cylinder. This tribo-set-up, installed on a lathe, can yield sufficiently high sliding velocities (several hundred m/min). It should be noted that the surface has to be regenerated prior to a new friction test.

The open tribometer was improved by Zemzemi et al. [230], and subsequently by Claudin et al. [60] so as to reach higher contact pressures and sliding velocities. In addition, it also provides, via special instrumentation, the heat partition at the interface, which is a key thermal parameter in numerical simulations of cutting.

In order to identify the appropriate friction model, several friction tests under the relevant sliding velocities and contact pressures must be carried out [184]. Because of the very high contact pressures, severe plastic deformation occurs. Hence, these tribometers measure an apparent friction coefficient that often overestimates the friction coefficient. Therefore, post-treatment of the test data is necessary to extract the relevant interfacial friction coefficient from the apparent friction coefficient as illustrated in Fig. 17. This identification can be performed through a numerical model of the friction test or through an analytical model based on geometrical observations of the scratches produced [60].

3.4. Other variables in friction identification

3.4.1. Effect of work material and its microstructure

Identification of the friction model by means of the experimental methods discussed in section 3.3 is fraught with challenges since friction depends on a large number of factors such as:

- work material composition and microstructure,
- cutting tool substrate, coating, surface texture, and
- lubricant composition and application technique.

Regarding the influence of the work material, Fig. 18 shows the frictional behaviour of a TiN coated carbide tool with apparent

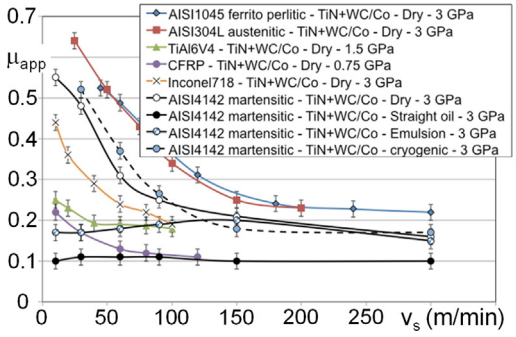

Fig. 18. Evolution of the apparent friction coefficient with sliding velocity for various material pairs [84,60].

friction coefficients μ_{app} that vary significantly from 0.1 to ~0.7. The differences between the work materials are significant for low sliding velocities under dry conditions. Ferritic-pearlitic and austenitic steels yield much higher friction coefficients compared to martensitic steels [95]. At high sliding velocities, the friction coefficients converge to lower values (~0.2). Moreover, all work materials with a similar microstructure do not satisfy the same friction model. For instance, a small percentage of CaMnS inclusions lowers the friction significantly at low sliding speeds, whereas similar inclusions do not affect the frictional behaviour of austenitic grades of steel.

3.4.2. Effect of cutting fluids

The influence of cutting fluids on the friction coefficient is shown in Fig. 19. It can be seen that the use of a lubricant oil causes a large decrease in the friction coefficient, especially at low sliding speeds. In contrast, the effect is reduced at higher sliding speeds compared to the dry case. In the presence of a lubricant, the friction coefficient remains constant around 0.1 irrespective of the sliding velocity (Fig. 19a). It should be noted that the friction behaviour strongly depends on the amount of lubricant supplied, its viscosity, and the contact duration. It was shown that the oil was evacuated in a few tenths of a second due the high contact pressure and sliding velocity [60]. On the other hand, oil will penetrate the tool-chip interface if the contact is longer than a second (turning, drilling, etc.). In interrupted cutting processes, the contact is lubricated before each cutting period. The amount of oil deposited at the interface (before cutting) depends strongly on the cutting speed. At high cutting speeds, the interface is starved of oil, which leads to dry sliding. In contrast, at low cutting speeds, the contact is fully lubricated. Moreover, oil viscosity strongly influences friction in MQL by modifying the generation of oil mist (droplet size and/or flow rate) irrespective of its composition (Fig. 19b).

The effects of liquid nitrogen (LN_2) or gaseous nitrogen and solid CO_2 on the lubrication mode and friction are still unclear. It has been reported that LN_2 significantly lowers friction in machining of Inconel 718, probably due to oxygen starvation [184]. In titanium machining, an oxidized surface strongly modifies the friction behaviour [60].

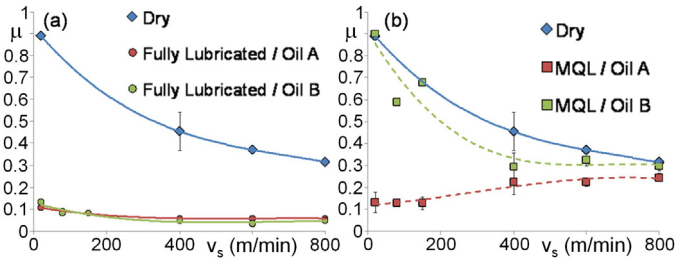

Fig. 19. Influence of lubrication and oil viscosity on friction: (a) full lubrication, (b) MQL [40].

3.4.3. Effect of cutting speed

Simulation of high speed machining at cutting speeds higher than 1000 m/min [92] needs friction data that are substantially modified by the strain rate and temperature. It was documented that friction coefficients for metallic work materials converge to 0.2 in dry sliding, which corresponds to a semi-solid friction regime as assumed in Ref. [164].

3.4.4. Effect of tool coatings

It is well-known that cutting tool coatings can significantly modify the frictional behaviour at the tool/work material interface [99,185]. The influence of the substrate is also very significant. It was shown in Ref. [231] that a CBN substrate yields a very low friction coefficient of 0.1–0.2 when machining Inconel 718, whereas TiAlN coated carbide tools exhibit μ values of 0.2–0.4. In contrast, HSS and carbides produce severe adhesion and high friction coefficients whereas PCD yields a self-lubricated contact when machining aluminium alloys [77].

An extensive characterization of tool coatings was reported in Refs. [99,91]. The characterization was based on mechanical, thermal and energy considerations according to the complex friction models reviewed in Section 3.2.

For difficult-to-cut alloys, operations that require specially coated tools are a key issue for both tool manufacturers and end users [202]. Typically, coatings are first deposited on samples, and tests and correlations between the outcomes of the laboratory tests and the results of cutting tests are established. In Refs. [202,203], methodologies for classifying the performance of cutting tool coatings were presented. For example, the ratio of ball wear area to the sample trace depth was used to rank the cutting performance of nanostructured TiN + AlTiN, TiN + AlTiN + MoS_2 and CrN + CrN:C + C coatings deposited on WC-Co inserts [202].

3.5. Implementation of friction in FE software

3.5.1. Friction effects in FE modelling of machining

As discussed earlier, the use of friction coefficients based on the Coulomb friction law to represent the contact conditions at the tool-chip and tool-workpiece interfaces for all cutting regimes is unrealistic. As a result, different friction models are often used in FE simulations of metal cutting.

In FE modelling of metal cutting, the local friction at the tool-chip interface is often modelled by the modified Coulomb friction law, where the friction stress is limited by the current shear flow stress of the work material $\tau_f = \min(\overline{\tau}, \mu\sigma_n)$ where τ_f is the friction (shear) stress, σ_n is the normal contact stress, μ is the local friction coefficient, and $\overline{\tau} = \overline{\sigma}/\sqrt{3}$ is the shear flow stress of the work material at the contact interface.

The dual zone idea was used to develop both numerical and analytical models for the tool-work contact friction. Moufki et al. [162] proposed the mean friction coefficient to be dependent on the mean temperature. Özlü et al. [174] used a friction model that separated the friction coefficient into two components—apparent and sliding friction coefficients. The first component is given by the ratio of the total friction and normal forces acting on the entire rake face whereas the second component is given by the ratio of the friction and normal forces acting in the sliding region.

To date, most of the analyses of tool-chip contact have dealt with the determination of the friction coefficient. Shi et al. [208] analysed the effects of a modified Coulomb friction law at the tool-chip interface via a 2D FE model for rake angles ranging from 15° to 30° and a friction coefficient ranging from 0.0 to 0.6. The maximum temperature, tool-chip contact length, shear angle, and the cutting forces were found to be strongly dependent on the coefficient of friction.

Arrazola and Özel [8] used the general purpose FE software ABAQUS (Explicit v6.1) to conduct a detailed sensitivity analysis of friction and other parameters in orthogonal cutting. They showed that, apart from the friction coefficient (μ), other input parameters such as the thermal conductance (K_I), the heat partition coefficient (Γ), and the percentage of friction energy transformed into heat (η) have significant influence on the results (see Table 4).

Among all the contact parameters, the friction coefficient had the greatest influence. However, it was observed that all contact parameters had a large influence on the maximum tool rake face temperature (T_o). It was found that (i) the friction coefficient was the only parameter that influenced the tool-chip contact length, and (ii) even for high values of the friction coefficient, the tool-chip contact length was lower than experimentally observed values. This could be a reason for the lower thrust force predictions commonly observed in FE simulations of metal cutting. In fact, these two aspects are major issues in FE modelling of chip formation, particularly when trying to model the effect of tool wear (especially, crater wear).

In order to solve this problem, Arrazola et al. [7] showed that the use of a variable friction coefficient decreased the errors between the simulated and measured feed/thrust forces to ~10%.

Table 4
Results of sensitivity analysis using ABAQUS Explicit 6.1 [8].

Effects of input parameters on numerical results									
Contact parameter	Ref. value	Range	Percentage change relative to results obtained using ref. value						ΔT = 50K
			T_O	ε^{pl}	H	t_2	F_c	F_f	
Thermal conductance (K_i)(W m^{-2} K^{-1})	10^8	10^3–10^8	−60	5	0	3	0	2	$1{\cdot}10^3$
Heat partition coefficient (Γ)	0.5	0.25–0.75	−60	0	0	1	0	0	0.05
Friction coefficient (μ)	0.23	0.2–0.5	−40	100	23	5	9	27	0.03
Friction energy trans. into heat (η)	1	0.7–1	11	2	0	−2	0	−1	0.12

T_o: max. tool rake face temperature (K); ε^{pl}: plastic strain in the chip; H: tool-chip contact length (mm); t_2: chip thickness (mm); F_c: cutting force (N); F_f: feed force (N); " − " before effect values indicates a decrease.

Arrazola and Özel [9] have studied the effect of Coulomb friction and sticking-sliding friction models on FE simulation of metal cutting. Key findings of their study are that the choice of the friction model has a greater effect on the thrust force while the cutting force is affected less. They concluded that sticking–sliding friction models should be used with caution and the limiting shear stress values must be determined for each cutting condition to predict the forces, stresses and temperatures more accurately in FE simulations.

Schulze et al. [200] implemented a modified friction model based on Coulomb's law with a variable friction coefficient that is a function of the relative sliding speed and temperature. This approach, which eliminates the proportionality between the friction stress and the normal stress, allows for modelling of the heat sources with greater accuracy and therefore simulation of the cutting induced phase transformations in the workpiece surface layers.

Childs [51] presented a detailed comparison of FE simulations of plane strain cutting with slip-line field models. A standard Coulomb friction law was employed at low normal contact stress levels while saturation of the friction stress was assumed at higher normal loads characterized by intimate contact and plastic flow. His results show that, in the absence of strain hardening and under heavily loaded conditions, the standard friction law $\tau_f = \min(\overline{\tau}, \mu\sigma_n)$ yields unrealistic results in that it predicts an increasing mean friction stress with cutting speed (and temperature), which contradicts the flow stress behaviour of the material.

Özel [170] investigated several friction models applicable to FE simulations of orthogonal metal cutting and concluded that a friction coefficient varying with normal stress provides better predictions of the cutting forces and tool stress distributions.

Haglund et al. [106] analysed the effect of six different friction models ranging from a constant friction model to a temperature dependent friction shear stress model in FE simulations of plane strain cutting of hardened steel. They found that all friction models underestimated the thrust forces even if the cutting forces were predicted accurately.

Ulutan and Özel [218] presented a "hybrid friction model" for the tool–chip contact where sticking and sliding contact parameters can be input to the FE simulation concurrently. As a result, computation of the tool stresses can be performed more accurately with integration of elastic and plastic deformations around all tool surfaces and, in particular, at the tool-chip and tool-workpiece contacts.

Atlati et al. [15] investigated the built-up-edge (BUE) formation and tribological behaviour at the tool–work material interface when cutting 2024-T351 aluminium alloy using a cemented carbide WC/Co tool. They proposed a new concept of time-dependent friction coefficient to represent varying contact conditions at the tool–work interface. They observed that the friction coefficient increased where adhesion on the rake face was expected.

Filice et al. [80] showed that, when the friction factor m is varied between 0.2 and 0.8, the simulated outputs in the orthogonal cutting of AISI 1045 steel are practically insensitive to the friction model used.

Bil et al. [34] proposed fitting the friction factor depending on the process variable simulated. They found that a friction factor m of 0.1 yields better prediction of the cutting force whereas the thrust force and the shear angle are predicted more accurately with a larger friction factor of 0.7. Three commercial FEM packages—MSC.Marc, DEFORM 2D, and AdvantEdge—were used. Negative thrust forces were predicted by DEFORM 2D. Hence, further improvements can be achieved by considering the dependence of the mean friction coefficient (or friction factor) on the mean contact temperature, as proposed by Moufki et al. [162].

3.5.2. Implementing friction models dependent on the local interface parameters

As showed by several authors, the tool-chip friction coefficient depends on the fundamental variables such as temperature, pressure, and sliding velocity [184]. However, most of the friction models implemented in FE simulations of the cutting process do not consider these effects. Such dependencies of friction can be implemented through the use of subroutines, such as VFRIC in ABAQUS Explicit.

To this end, Atlati et al. [16] employed the VUINTER subroutine in their FE simulations of the cutting process where they considered the influences of sliding velocity, cutting temperature, and local properties of the tool-workpiece interface on the friction coefficient. A good agreement with experimental results was observed, except for the thrust force which was underestimated. Bonnet et al. [36] have included the influence of sliding velocity by means of the arbitrary Lagrangian-Eulerian approach in ABAQUS (Explicit). Their results showed significant improvement in the predicted quantities over a large range of interfacial sliding conditions.

The VFRIC subroutine in ABAQUS (Explicit) was also used by Courbon et al. [64]. They obtained improved predictions of the feed force and better descriptions of the distribution of temperatures on the rake face and of the heat flux into the tool. In addition, Courbon et al. [64] showed that it was possible to predict microstructure evolution in the chip due to recrystallization and other physical effects.

3.6. Friction modelling with tool wear effect

Friction and wear are two types of interactive responses of the tribo-system that occur simultaneously between two moving surfaces, e.g. between the chip and the tool. Experiments suggest that low wear is characterized by low friction while high wear is characterized by high friction.

This relationship has not yet been sufficiently investigated. From a practical point of view, special attention should be given to coated cutting tools [110,92]. Fig. 20 shows the evolution of the friction coefficient for TiN coated samples using a ball-on-disc tribo-tester at a normal load of 200N. Three characteristic stages are evident: low friction stage (I), ploughing friction stage (II), and coating breakdown stage (III). The friction coefficient in stage (I) ranges from 0.15 to 0.2.

The second group of investigations of friction evolution during wear tests concern machining processes, including orthogonal and oblique machining of a spheroidal cast iron using ceramic Si_3N_4 and CBN cutting tools [100,98], and hard machining of a case-hardened alloy steel using CBN tools [93]. The local values of friction coefficient corresponding to various levels of tool flank

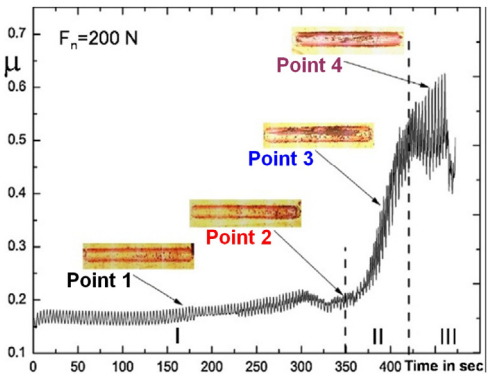

Fig. 20. Friction coefficient evolution for TiN coated sample at 200 N load [153].

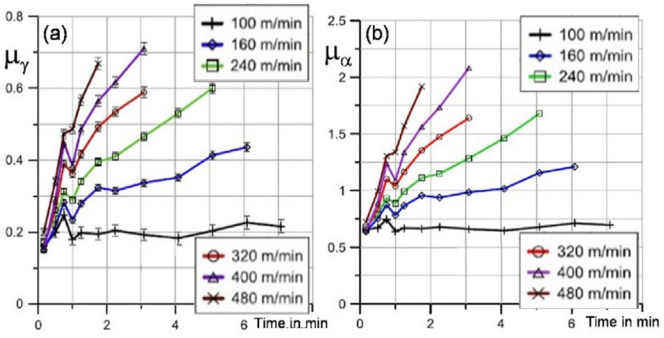

Fig. 21. Changes in friction coefficient at the (a) rake and (b) flank faces [98].

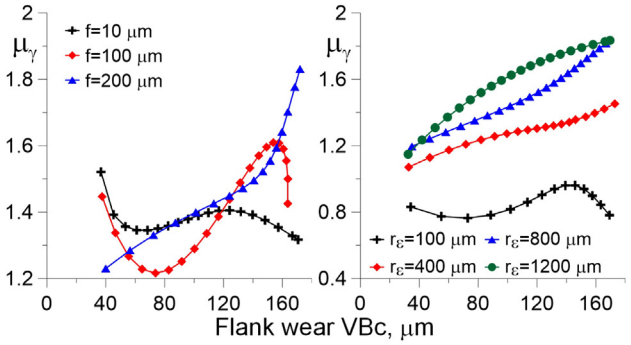

Fig. 22. Changes in the friction coefficient with tool wear due to variations in the (a) feed rate, and the (b) tool nose radius [93].

wear (VB_c) were determined using a mechanistic friction model and the equivalent rake angle, which was determined graphically from microscope images [100]. The observed changes in the friction coefficient at the rake and flank faces are shown in Fig. 21.

At the rake face, μ_γ changes from about 0.15 to 0.75 depending on the wear (Fig. 21a). Changes in the flank face friction coefficient μ_α are distinctly higher and range from 0.55 to about 2 (Fig. 21b). They are caused by the adhesion of the tool to the chemically fresh workpiece surface. A good agreement between μ_α in machining and in the corresponding tribo-tests was observed [100].

The investigation of hard machining using CBN cutting tools was focused on the separation of the ploughing component of the friction coefficient, which is dominant at extremely low uncut chip thickness (~2.5 μm) [93,94]. As shown in Fig. 22, large increases in the friction coefficient were observed at higher feeds (Fig. 22a) and large tool nose radii (Fig. 22b). Large values (~4) of the friction coefficient were also reported in Ref. [110].

The main conclusion from the wear-based studies is that tool wear influences friction differently, and adhesion or ploughing has a predominant effect on the friction coefficient.

3.7. Future needs and opportunities

1. A comparative assessment of the accuracy of existing friction models used in the simulation of metal cutting.
2. A detailed analysis of the interaction between the friction model and the constitutive model used to simulate metal cutting.
3. Development of more effective tribo-meters capable of accurately reproducing the frictional conditions in machining under contact different conditions.
4. Improved understanding of the effects of cutting fluids, tool coatings, and tool wear on friction and ways of incorporating their effects into friction models.
5. Development of experimental methods for separating the adhesion and ploughing components of friction for different tribo-pairs.

4. Thermal data and models

The thermal aspects of machining play a central role in modelling and simulation of metal cutting. They affect thermal distortion, plastic deformation associated with chip formation, machining-induced residual stresses, and thermal damage. It is well established that thermally induced errors in machining have been accorded an equal place with other factors, namely tool wear and deflection, and can contribute more than 50% of the total machining error. The accuracy of cutting process simulation is dependent on the accuracy of the heat transfer model, including the temperature-dependent physical and mechanical properties of the material. There are two important thermal issues that need to be carefully considered—the *thermal boundary conditions* and the *heat partition* ratios between the chip, tool, and workpiece. This section of the paper provides a detailed review of these two issues and how they relate to emerging technologies, e.g., MQL, cryogenic cooling, and vibration-assisted drilling.

4.1. Thermal and physical properties of materials

The basic thermal data required for modelling and simulation of machining are the thermal conductivity k, the specific heat c_p, the coefficient of thermal expansion β, and the density ρ. Two combinations of these basic properties are of special significance in heat conduction (a) the thermal diffusivity α ($=k/c_p\rho$), which is a measure of the ability of the material to conduct thermal energy relative to its ability to store it, and (b) the thermal effusivity $b = \sqrt{kc_p\rho}$, which is a measure of the rate at which the material can absorb heat i.e., it is a measure of the thermal inertia of the material in the transient state. The low value of b for titanium alloys explains their high cutting temperatures, compared to other materials, e.g., steels, cut under the same conditions [207].

Sensitivity analysis carried out by Arrazola and Özel [8] showed that the thermal conductivity (k) and specific heat (c_p) of the workpiece material have as much influence on the temperatures as the material flow stress or the friction at the tool-chip interface. A differential scanning calorimeter [177] is used to measure the change in c_p with temperature and the transition temperatures, such as phase transformation, while the laser flash method is the most common method for measuring thermal diffusivity α and conductivity k [176]. The coefficient of linear thermal expansion β, which has a direct effect on the thermal elastic deformation and thermally-induced residual stresses, is commonly measured using the mechanical dilatometer method [155]. Knowing β for a given sample geometry, one can readily establish the variation in density with temperature T as $\beta = \Delta V/(V_o \cdot \Delta T) = -\Delta\rho/(\rho \cdot T \cdot \Delta T)$.

An example of the dependence of c_p, ρ, α, and β on temperature for C45 steel is shown in Fig. 23. The figure shows that ~300% increase in c_p is observed from room temperature to 700 °C. Data concerning the relevant temperature-dependent properties of metallic and ceramic workpiece and tool materials are readily available in the literature, e.g., Refs. [178,109,217,88,83,216].

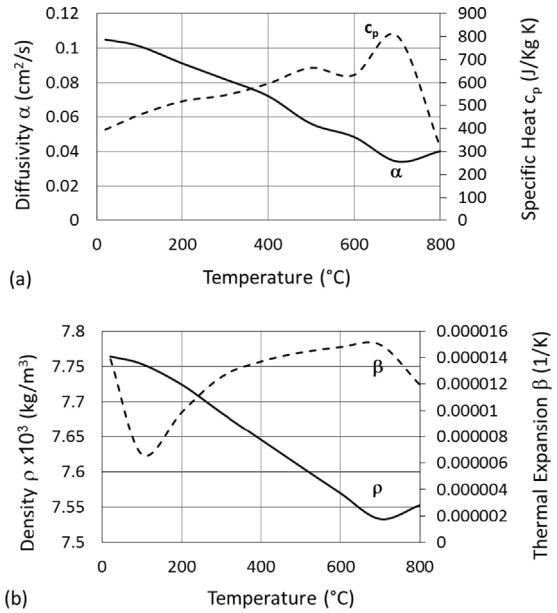

Fig. 23. Effect of changes in (a) thermal diffusivity α and specific heat c_p, and (b) density ρ and coefficient of linear thermal expansion β [6].

4.2. Thermal boundary conditions

4.2.1. Convection heat transfer around rotating bodies

The convective coefficients of heat transfer (CHT) h around rotating workpieces and tools are frequently needed for simulating certain cutting processes. This problem has been investigated experimentally by many researchers, e.g., Refs. [3,75,71,33,173]. The CHT h data is commonly expressed in terms of the dimensionless Nusselt number (Nu), and as a function of other dimensionless numbers including the Reynolds (Re) and Prandtl (Pr) numbers (for forced convection):

$$Nu = hl/k_f = f(Re, Pr) \tag{20}$$

where l is the characteristic length of the rotating body, k_f is the fluid thermal conductivity, while Re and Pr depend on l, the mass flow rate m, and the thermophysical properties of the cutting fluid and the target material. For ambient air, $Pr = 0.72$, and this equation becomes:

$$Nu = CRe^n \tag{21}$$

where C is between 0.1 to 0.318 and n is between 0.57–0.7 for Re values that range from 0.08×10^4–10^5 [195,101,138,165,129]. As Fig. 24 shows, for a cylindrical body (d = 100 mm) rotating at n = 10,000 rpm, h is in the range of 25–40 W/m^{2}K. In the case of convection heat transfer in narrow gaps of thickness g, which is encountered in vibration-assisted machining for example, Nu is also a function of the ratio G between the gap thickness and the radius of the rotating part r; $Nu = f(Re,G)$ [190]. With increase in G and n, the laminar air flow changes and toroidal Taylor vortices can form, thereby enhancing the heat transfer. A CHT of 150 W/m^{2}K can be reached [190]. A similar effect of Taylor vortices is also expected in orbital drilling [191].

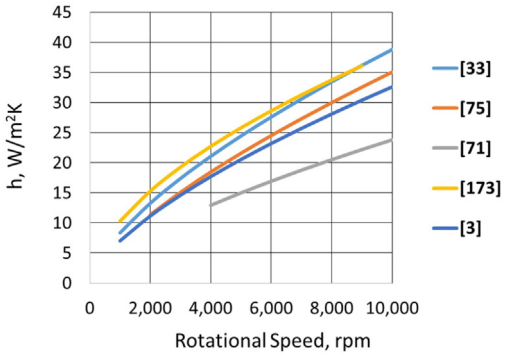

Fig. 24. Effect of rotation speed on the CHT (for d = 100 mm); data compiled from [3,75,71,33,173].

Experimental determination of the CHT h requires inserting a number of thermocouples into the rotating body [135] and then using FE analysis to solve an inverse heat conduction problem. Recently, Attia et al. [19] proposed a method that relies on measuring the temperature at a single location on the surface for determining h through closed form solution of a direct heat conduction problem.

4.2.2. Coolant flow and forced convection heat transfer

To control the cutting temperature T_c, cutting fluids are applied in the directions marked A–D (see Fig. 1). While the fluid delivery in direction D and impingement on the tool represents a condition of "free flow" (or open flow), directions A (rake jet), B (flank jet) and C (transverse rake jet) represent the condition of "confined flow". This distinction has strong influence on the dynamics of fluid flow and the mechanism of heat transfer.

4.2.2.1. Free flow condition. The open flow field of an impinging jet consists of three regions [237]; the *free jet region* with a 'potential dense core' (L/d = 4–6), *the stagnation region* and the *wall jet region*, where the flow is in the outward radial direction. In this region, the boundary layer developed from the stagnation point has a strong effect on the heat transfer rate. The cooling area covers ~12–20d in the moving direction and 8–15d in the lateral direction, where d is the nozzle diameter [46]. With an increase in the relative velocity between the jet and the moving target, the cooling length is shortened in both the moving and lateral directions [47]. Therefore, the distribution of CHT in the cutting zone, and not its average value, should be modelled.

When the surface temperatures are higher than the coolant saturation temperature, boiling may occur and the peak CHT may reach 150–200 kW/m^{2}K at the jet impingement centre for a round/slot jet. This scatter in the CHT data is attributed to the variance in the peak or average values, differences in the nozzle, the presence of flow confinement, turbulence upstream from the jet nozzle, and whether single phase, nucleate, or film boiling are encountered [46,120].

The coefficient of heat transfer h resulting from jet impingement also depends on the nozzle-to-target distance (L/d), and the displacement from the stagnation point (r/d): $Nu = f(Re, Pr, L/d, r/d)$. In addition, the effects of nozzle geometry, flow confinement, and turbulence have all been shown to be significant. The results reported in Refs. [120,183] showed that within the range $2 < L/d < 12$ the local heat and mass transfer are independent of (L/d) at radial positions $r/d > 4$–6. For convection in the impingement region of a single-phase, water-based coolant, it was shown that the peak CHT is nearly the same for stationary and moving target surfaces (at $v < 0.5$ m/s) with a jet velocity of 2.3 m/s [47]. Experimental data for the CHT for impinging turbulent jets from a circular nozzle onto a plane surface for $1.2 < r/d < 16$ and $5000 < Re < 124{,}000$ have been collated in Refs. [237,120,147].

4.2.2.2. Confined flow condition. In restricted or confined flow, the presence of a wedged opening (or crevice) introduces another dimension to the problem complexity, since heat conduction in the narrow gap can be the dominant mechanism, as demonstrated by Attia and D'Silva [18]. A solution to this nonlinear problem, which involves subcooled nucleate boiling, is to determine if nucleate boiling is taking place in the crevice region. Another type of flow restriction is encountered when the jet from a tube is confined in a larger tube. In this configuration, a very rapid 180° change in the flow direction causes a strong change in the fluid momentum, leading to intensive perturbation of the heat transfer surface [234].

4.2.2.3. Effect of jet inclination and coolant flow rate. The general profile of the CHT along the radial direction of the target surface

can be described by the following exponential function, where the maximum value is at the intersection of the jet axis with the surface: $Nu \propto 1/exp(A + B\ cos\ \phi)\ (r/d)^m$, where ϕ is the jet inclination angle [87]. The coefficients A and B for various jet parameters are given in Ref. [141] where this formulation was used to derive correlations between the jet-flow rates in the overhead and flank directions (B and D in Fig. 1) and the corresponding CHT h. It was shown that increasing h by n times in the regions B and D requires increasing the coolant flow rate by approximately as much as $n^{1.5}$ and n^2. These models show that in both cooling directions, the corresponding percentage reductions in the temperatures of the cutting regions are much smaller than the percentage increase in coolant flow rate, as confirmed by FE simulations [142]. Childs et al. [54] estimated the CHT of a water-based flank jet to be 10^3–10^4 W/m^{2}K in the direction B. They showed that the tool temperatures are sensitive to changes in the CHT in this practical range, thus underlining the importance of cutting fluid formulation, supply rate, and direction of application. For an *air jet*, Sagot et al. [195] suggested the following correlation for estimating the average CHT on a target surface for $10^4 \le Re \le 3 \times 10^4$, $3 \le r/d \le 10$ and $2 \le L/d \le 6$:

$$Nu = 0.0603Re^{0.8}\left[1 - 0.168\left(\frac{r}{d}\right) + 0.008\left(\frac{r}{d}\right)^2\right] \times \left(\frac{L}{d}\right)^{-0.037} \quad (22)$$

Data for the effect of nozzle shape on the local CHT of an impinging air jet are also available [101,138]. Detailed surveys of the impingement cooling effect of an air jet are given in Refs. [165,120].

In creep-feed grinding, the CHT in the grinding zone for high flow rate flood cooling were estimated to be 15,000–20,000 W/m^{2}K [129]. For high efficiency deep grinding, the CHT were estimated to be 10,000 W/m^{2}K for oil-in-water emulsions and 4000 W/m^{2}K for neat oils [189]. Coefficients of heat transfer of 37,000–43,400 W/m^{2}K were reported for water-based coolants in grinding, as compared to 900–1500 W/m^{2}K for minimum quantity lubrication/cooling (MQL) [104,105]. For spray cooling in grinding, the following semi-empirical model was proposed to estimate the average heat transfer coefficient [104,206]: $Nu = 0.664Pr^{1/3}Re^{1/2}$. Much higher values of h were reported in Ref. [125] with up to 6.0×10^5 and 1.7×10^6 W/m^{2}K for oil and water-based coolants, respectively, and high grinding wheel speeds of up to 100 m/s. The CHT is critically dependent on the fluid film thickness within the contact zone, which depends on the wheel speed, porosity, grain size, coolant type and flow rate, and nozzle size. This model is applicable to a wide range of grinding regimes, including deep grinding with large contact lengths, and conventional shallow cut grinding.

4.2.2.4. Coefficient of heat transfer in cryogenic machining. Cryogenic machining can significantly improve tool life and productivity of metallic components [73]. The gas dissolved in the liquid increases the heat transfer in subcooled boiling. The average Nu for a jet impinging on a circular plate is proportional to ($Re^{0.45}\ Pr^{1/3}$) [29]. Heat transfer in liquid nitrogen (LN2) jet systems was also investigated by Dreitser [70] for a wide range of nozzle diameters and flow rates. The CHT was found to be 1.7×10^3–6.5×10^3 W/m^{2}K, i.e., 10–40 times higher than in boiling under natural convection. It was also concluded in Ref. [148] that at the tool-chip separation point, the surface CHT is very small and rapidly increases with distance (Fig. 25).

The surface CHT in the open region can reach 5×10^4 W/m^{2}K, more than an order of magnitude higher than typical convection cooling. Recently, computational fluid dynamics analysis of multiphase flow of LN2 was carried out for a nozzle diameter, d = 1 mm, a flow rate = 1 l/min, and at a distance L = 15 mm from a hot surface at 700 K [72]. The CHT at the intersection of the hot target surface with the centreline of the jet was estimated to be 4.9×10^4 W/m^{2}K. It is also worth noting that nucleate boiling data for LN2 for pool and forced convection boiling [67] can be used to establish the fully developed region of the boiling curve in forced convection [61]. Fig. 26 contains a compilation of some of the relevant data published in the literature for the range of CHT values. For the sake of comparison, typical CHT values for free and forced convection in a single flow regime, MQL, and air quenching are also presented, along with those for metal-to-metal thermal contact conductance.

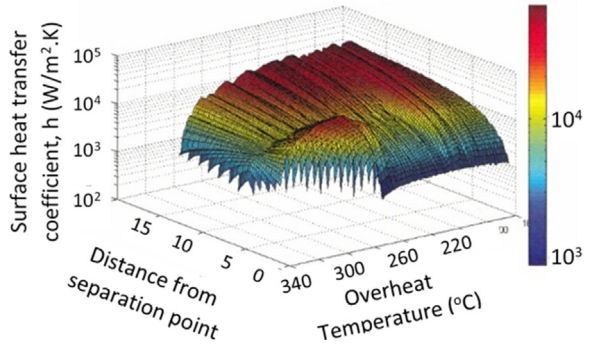

Fig. 25. Surface heat transfer coefficient at 51.7 kPa driving pressure [148].

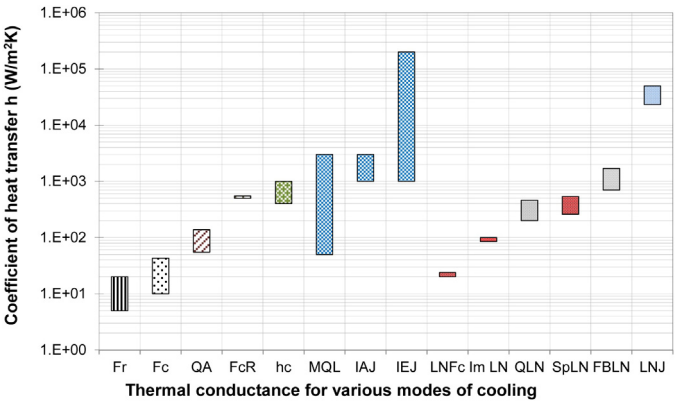

Fig. 26. Typical values of CHT in various cooling regimes. Fr: free convection in air/GN. Fc: forced convection. QA: air quenched. FcR: on rotating parts in air. hc: thermal contact conductance. MQL: min. quantity lubrication. IAJ: impinging air jet. IEJ: impinging emulsion jet. LNFc: LN flowing on plate. ImLN: immersed in LN, QLN: quenched in LN, SpLN: splashed with LN, FBLN: film boiling in LN, LNJ: LN jet [122].

4.3. Thermal contact conductance

Due to the nature of real surfaces, the physical and tribological interactions between contacting solids are limited to the highest asperities. As a result, frictional heat generated at the micro-contact areas will spread out rather than taking a straight path. This gives rise to the so-called thermal constriction (or spreading) resistance. To overcome this resistance, a steep temperature gradient has to be established in the subsurface layer, giving rise to high contact temperatures and thermal stresses. This process is further complicated if surface coatings are present, since the divergence of heat flow lines takes place partly in the coated region and partly in the base material.

Coated tools are commonly used today to improve tool life and reduce friction. For machining simulation and for proper coating design (type, number of layers, order, thickness), the thermal performance of the coated layers needs to be assessed. The experimental data reported in Refs. [133,96] indicate that the thermal properties of coatings have significant effect on the heat partition ratio, and the temperature field in the substrate. However, using FE modelling, where the thermal contact conductance at the tool-chip interface h_c was assumed to be infinity (perfect contact) [130] or a constant value of the order of 10^4–10^6 W/m^{2}K or higher [82,225,168,63], a contrary conclusion was reached. The theory of nonlinear thermoelastic behaviour of contacting solids, developed by Attia and Kops [21,20,22,23], can

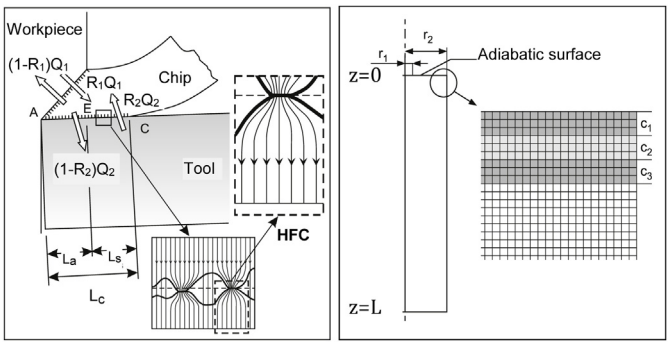

Fig. 27. (a) Schematic of the contact configuration at tool-chip interface, (b) FE model of the heat flow channel [24].

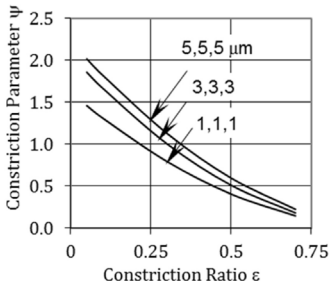

Coating type	t	α	β
uncoated tool	-	0.953	1.65
TiN-Al_2O_3-TiC	3,3,3	2.837	1.79
TiN-TiCN-TiC	3,3,3	2.060	2.00
TiN-TiCN-TiC	1,1,1	1.618	2.00
TiN-TiCN-TiC	5,5,5	2.226	1.90
TiN-TiCN-TiC	0,3,3	1.640	1.88
TiN-TiCN-TiC	0,0,3	1.347	1.74
TiC-TiCN-TiN	3,3,3	1.637	1.65

Fig. 28. (a) Effect of coatings on the constants of Eq. (23) for different thicknesses t (in μm), see table, (b) Ψ –ε relationship for TiN-TiCN-TiC coating with different thicknesses t (in μm) [25].

provide an explanation for these seemingly contradictory conclusions. To model the thermal constriction phenomenon at the interface, one has to consider the *distribution* of the contact pressure, and consequently the thermal contact conductance, over the interface (and not their average value), as they play a critical role in *redistributing* the heat flux across the interface. It was shown in Refs. [22,23] that only under this condition the process modelling will agree with experimental observations and reveal the significant effect of thermal contact conductance on the temperature field, and on the thermal response of the system. The thermally disturbed zone due to the constriction (or divergence) of the heat flow lines is confined to a very shallow subsurface layer of the order of 50–100 μm [24]. Sensing the temperature at much larger distances will not reveal this phenomenon. This may explain the conclusion drawn from the experimental results reported in Ref. [186], which suggested that coatings have insignificant thermal effect. In this work, a single temperature sensor was located between the insert and the insert holder to solve an inverse heat conduction problem and estimate the heat input to the tool.

The analysis carried out by Attia and Kops [24] provides a methodology for modelling and generating data for the distribution of h_c along the interface between the chip and a multi-layer coated tool, considering the asperity level contact mechanics. Fig. 27a depicts an idealized orthogonal cutting process with a sharp tool, where two heat sources are present; the primary shear plane source Q_1 and the rake face source Q_2. The latter represents the secondary deformation zone in the chip and the tool-chip friction. In the sliding zone (l_s), the heat generated enters the tool through a limited number of small contact spots, whose radii r_1 are dependent on the local contact pressures p_c. The volume, which encompasses each of these micro-contacts and extends some distance into the solid, is defined as the elemental heat flow channel (HFC). Since the HFCs are connected in parallel, the solution of the heat transfer problem in a single channel represents the building block for the whole process. Through FE analysis, the thermal constriction for a HFC can be estimated (see Fig. 27b, with three layers of coatings; c_1, c_2, c_3).

The constriction ratio $\varepsilon = r_1/r_2 = p_c/\sigma_f$, where σ_f is the flow stress of the softer workpiece material. By applying heat flow rate Q_c over the micro-contact ($0 \le r \le r_1$), the difference between the average temperatures of the micro-contact and the HFC cross section ($0 \le r \le r_2$) at $z = 0$, ΔT_c, is the driving force required to overcome the constriction resistance: $R_c = \Delta T_c/Q_c$. In this analysis, it is imperative to consider the temperature-dependence of the thermal and mechanical properties of the coatings and substrates. These data were collected from different sources and are summarized in Refs. [96,76,89].

The constriction resistance is commonly expressed in the following dimensionless form: $R_c = \psi/4kr_1$, where ψ is the constriction parameter. The thermal and mechanical contact problems are linked by the following expression [227]:

$$\psi = \alpha(1-\varepsilon)^{\beta} \tag{23}$$

Examples of the effect of the coating architecture on the $\Psi - \varepsilon$ relationship are given in Fig. 28. In calculating Ψ, the thermal conductivity of 'WC' was selected as a reference value. The significant increase in the constriction resistance (Ψ) with the reduction in contact pressure (ε) is evident. From the analysis presented in Ref. [24], the total thermal constriction resistance R_c is given by the following equation:

$$R_c = \left(\frac{\sqrt{2\pi}}{A_a}\right)\left(\frac{\overline{\sigma}}{|\overline{m}|}\right)e^{x^2}\left[\frac{\alpha_1(1-\varepsilon)^{\beta_1}}{k_1} + \frac{\alpha_2(1-\varepsilon)^{\beta_2}}{k_2}\right] \tag{24}$$

where A_a is the apparent macro-contact area, while $\overline{\sigma}$ and $|\overline{m}|$ are the standard deviation of the asperity heights and the mean absolute slope of the asperities of the equivalent surface, respectively, and $\overline{\sigma} = \sqrt{\sigma_1^2 + \sigma_2^2}$ and $|\overline{m}| = \sqrt{m_1^2 + m_2^2}$. The parameter x is the ratio of the separation between the median planes of the contacting surfaces and $\overline{\sigma}$.

For $1.5 < \varepsilon < 2.0$ and a practical range of contact pressures $p_c/\sigma_f < 0.01$, the following equation can be used to estimate the distribution of the thermal contact conductance at the tool-chip interface h_c as a function of the contact pressure distribution p_c:

$$h_c = \frac{|m|}{0.136\sqrt{2\pi}\overline{\sigma}}\left[\frac{\alpha_1}{k_1} + \frac{\alpha_2}{k_2}\right]^{-1}\left[\frac{p_c}{\sigma_f}\right]^{0.97} \tag{25}$$

This equation was validated by reducing it to the experimental and analytical cases investigated in Refs. [227,226,198] for uncoated surfaces and for single layer coating.

It was shown in Ref. [24] that treating the coating merely as a thin layer of thermal resistance between solids in perfect contact, as presented in Ref. [161], leads to a significant error. Compared to no coating and perfect contact over the full contact length, the results reported in Refs. [24,25] showed that with a TiN/Al_2O_3/TiC coating and the presence of thermal constriction resistance, the maximum temperature T_{max} may be reduced significantly causing a drop in the WC tool hardness from 57 to 52 HRC, and the location of T_{max} may shift from the cutting edge to the extreme point of contact. Simulation of steel machining showed that h_c typically varies between 0 and 2–3 × 10^3 kW/m^2K along the chip-tool interface [128]. Recognizing the importance of the spatial variation of the contact conditions at the interface, Courbon et al. [62] introduced a model where the coefficient of friction μ and the heat partition ratio η are variables and they depend on the local sliding velocity v_s. The v_s–η relationship was extracted from pin-on-disc friction experiments. The model confirmed the sensitivity of the temperature field on the local variation along the tool-chip interface. It assumed, however, that the thermal contact conductance h_c is constant ($h_c = 10^4$ W/m^2K) and ignored the thermal constriction due to the tool coating. The approach proposed by Grzesik and Nielsony [97] for modelling the interface temperature in machining with multilayer coated tools considered only the thickness and thermal properties of the coating but ignored the constriction phenomenon. Careful analysis of the results presented in Ref. [198] shows that the thermal resistance of a coating is not only dependent on its thickness δ_c and thermal conductivity k_c, but also on the ratio of the coating thickness-to-the micro-contact

radius δ_c/a_{mic} and the ratio of its thermal conductivity to that of the tool (substrate), k_c/k_t. Therefore, the change in coating thermal conductance h_c is not linearly proportional to k_c/δ_c, but may lead to a much greater effect.

4.4. Future needs and opportunities

1. Physically-based modelling of the thermal constriction phenomenon at the tool-chip interface, considering the nonlinear thermoelastic behaviour of the system, and the texture, crystal orientation, and coating architecture. This allows the development of a data-base for tool design and accurate simulation of the machining process.
2. Development of non-intrusive measurement system/technique for determining the distribution of the heat transfer coefficient in various regions of the cutting zone under various modes of cooling, and its correlation to process variables.
3. CFD modelling of cryogenic, MQL, and high pressure coolant delivery for enhanced dissipation of cutting energy.

5. Microstructure data and models

5.1. Microstructure evolution in machining

Microstructure evolution in the machining of crystalline metals and alloys is largely governed by the prevailing mechanics of material removal and the resulting chip formation. Microstructure evolution for continuous and other chip formation types occurring in the machined surface/subsurface are reviewed below.

5.1.1. Microstructure evolution in the machined chip

Deformation during continuous chip formation encompasses a wide range of strains, strain rates and temperatures that together influence the operative micromechanics of plastic deformation. Depending on the thermomechanical variables and material system parameters, microstructure evolution may be governed by mechanisms mediated by conventional dislocation slip and glide, deformation twinning, and/or solid state phase transformation. For dislocation mediated-plasticity, microstructure evolution is classified into multiple operative thermally-activated and/or mechanically-activated processes including recovery, continuous/discontinuous recrystallization and grain growth. At low homologous temperatures and strain rates, microstructure recovery and recrystallization occurs at relatively low to moderate strains. Microstructure refinement in fcc metals has been reviewed by Hughes and Hansen [114] and includes the generation of dislocations, their rearrangement into low energy cellular structures and subgrain boundaries, formation of lamellar boundaries and rotation to form high energy, high angle grain boundaries.

For machining processes, this evolution has been observed directly in chip formation for fcc metals and alloys, including those based on copper, nickel and aluminium. For example, Brown et al. [37] showed direct relationships between the formation of various microstructures in the machined chip and the machining parameters, including rake angle and cutting speed, which together affect strain, strain rate and temperature, as shown in Fig. 29. Saldana et al. [196] expanded on these results and determined differences in the evolution of the machined microstructures at low homologous temperatures (e.g., cryogenic), including mechanisms for the enhanced refinement of the microstructure. In addition to the stable evolution of microstructure by continuous recrystallization, discontinuous recrystallization and grain growth also contribute within specific thermomechanical parameter ranges. For example, higher machining temperatures can result in discontinuous dynamic recrystallization in the chip due to nucleation and growth of new strain-free grains throughout the deformed microstructure. This has been observed at high machining speeds that result in high effective strain rates in the deformed chip [37]. Additionally,

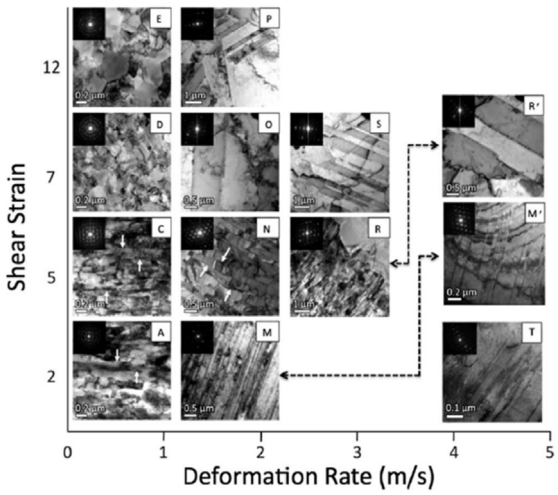

Fig. 29. Microstructures obtained in machining with varying rake angles and cutting speeds designed to yield differences in strain, strain rate and temperature [37].

mechanically-activated grain growth (or coarsening) also has been observed at low strain rates and high effective strains [37].

While the above phenomena (e.g., continuous/discontinuous recrystallization, grain growth) have been observed when initial microstructure is in the microcrystalline regime, it also has been recognized by Basu and Shankar [30] that length scale effects lead to limited dislocation generation and refinement at small length scales wherein the machining volume approximates crystal size.

In addition to deformation mediated by conventional dislocation slip, deformation by mechanical twinning is an alternative deformation mode often observed in machining of low stacking fault energy (SFE) fcc as well as in bcc and hcp metals. Deformation twinning involves coordinated motion of atoms within a single grain, resulting in reflection of the original lattice in the twinned volume. Twinning generally occurs when limited slip systems are available to support plastic deformation and in situations wherein the stress to cause twinning is less than that required to cause slip. Conditions wherein these modes are promoted involve both high strain rates and low homologous temperatures. Brown et al. [37] and Saldana et al. [196] demonstrated formation of deformation twins under such conditions for various fcc metals, including copper and brass. Deformation twins also have been observed in the machining of other low SFE metals and alloys, including steels, magnesium-based alloys, and titanium-based alloys [204,124,192]. In addition to deformation twinning, solid-state phase transformations have long been known to also play a major role in microstructure evolution for structural steels in terms of martensitic white layer formation both in the chip and in the machined surface. In this regard, martensite forms due to simultaneous effects of high strains and high temperature gradients in the machining of steels.

Deformation occurring in discontinuous chip formation, such as in serrated chip formation observed in titanium alloys, exhibits more complex microstructure evolution due to the occurrence of strain heterogeneities caused by shear banding in the machined chip. This is most clearly observed in machining of titanium alloys, magnesium alloys, and nickel superalloys where the chip is characterized by periodic occurrence of two microstructure regions: (1) a region of transient plastic deformation where the original microcrystalline grain structure is observed, and (2) a highly localized and refined shear band region [132]. In the case of MgAZ31B shown in Fig. 30, the former region consists of microcrystalline grain boundaries which can be resolved metallographically, as well as evidence of grain-level plastic deformation in the form of deformation twins and heavily defected subgrain regions [194]. The shear banded region is metallographically featureless and consists of refined nanocrystalline and/or ultrafine grains [194]. While microstructure refinement and the nature of shear bands are not completely understood, the formation of these

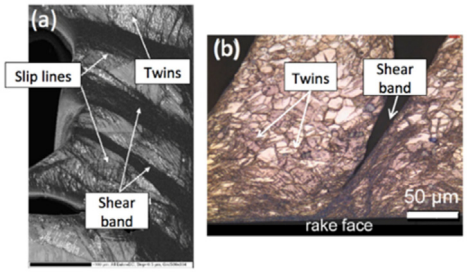

Fig. 30. Shear banding and twinning in (a) AISI 316L and (b) MgAZ31B chip [194,152].

microstructures are ultimately linked to grain refinement by continuous dynamic recrystallization.

5.1.2. Microstructure evolution in the machined surface

The microstructure evolution in the machined surface and in the secondary shear zone follow processes similar to that described above for the primary shear zone, albeit in a more heterogeneous manner due to greater heterogeneity in thermo-mechanical loading in these regions. In the secondary shear zone, severe straining due to high friction at the tool-chip interface gives rise to enhanced grain refinement. The thermomechanical history of the machined subsurface closely matches the deformation occurring in the deformed chip. In terms of continuous recrystallization, Calistes et al. [42] showed that microstructures near the machined surface closely resembled microstructures formed in the interior of the chip volume for various fcc metals. These microstructures were found to be ultrafine-grained and were similar in size to that observed in the machined chip. The similarity in microstructure for these different regions is expected as deformation strain decays into the subsurface, wherein the deformation at the machined surface is similar to that of the machined chip [102]. More recently, Basu et al. [32] showed relationships between the mechanics of surface generation in periodic topographies and the depth of the refined microstructure layer formed by continuous recrystallization, as well as the resulting spatial gradient in grain size. The resulting ultrafine-grained microstructure in the machined surface is correlated with the subsurface strain profile as well as locally-varying strain path changes in the machined surface.

The deformation heterogeneity in the machined subsurface also can provide conditions necessary for deformation twinning. Due to the strong influence of strain, strain rate and temperature on the likelihood of twinning, deformation twinning is also strongly strain dependent, forming at low strains and being eliminated at high strains. In this regard, deformation twinning is unlikely to occur in the immediate machined surface, which is associated with high strains and is more likely to occur at greater subsurface depths at low strains. M'Saoubi and Ryde [152] and Shankar et al. [204] showed this through electron backscatter diffraction and metallographic observations of deformation twins in the machined subsurface for machining of austenitic stainless steel and titanium, respectively. Twins also readily form under low temperature cryogenic conditions in many materials. Pu et al. [179] showed cobalt chrome and magnesium alloys exhibit deformation twinning in the subsurface under cryogenic burnishing and machining, respectively.

5.2. Measurement of microstructure

Measurement of microstructure variables in machining must be able to resolve small domains at the grain-level. Conventional methods for characterizing microstructure over large, non-site-specific chip and machined surface regions, including scanning electron microscopy (SEM) and electron backscatter diffraction (EBSD), have been summarized by Jawahir et al. [123]. More recently, advances have been made to apply site-specific methods based on transmission electron microscopy (TEM) and focused-ion beam (FIB) milling for high-resolution observation of microstructures in the chip and the machined surface. TEM involves accelerating electrons through thin sample volumes for measurement of the crystalline structure. Image contrast in the TEM is used to quantify microstructure in the machined chip and surface, including measurement of grain size, dislocation density, and grain boundary morphology. TEM-based selected area diffraction (SAD) enables visualization of the spread in crystal orientations or to directly map grain orientation by sample tilting and rotation. For site-specific observations, samples are produced by direct energy-based localized removal of material from highly specific regions. FIB liftout involves use of a precision nanomanipulator and FIB milling to remove a localized piece of material [86]. First, an ion source and user-defined masks are used to locally ablate material from a work surface in the form of a two-sided trench with a centre wall forming the final sample. The centre wall is protected using platinum depositions applied to the work surface. A nano-manipulator is brought in contact with and welded to the centre wall. After removing the centre wall from the workpiece, the sample is thinned successively using the ion beam. These methods, when coupled with lower-resolution measurement methods based on PIV/DIC and SEM/EBSD, have been used recently by Sagapuram et al. [193] to make highly localized measurements of microstructure within Ti–6Al–4V shear bands, as shown in Fig. 31.

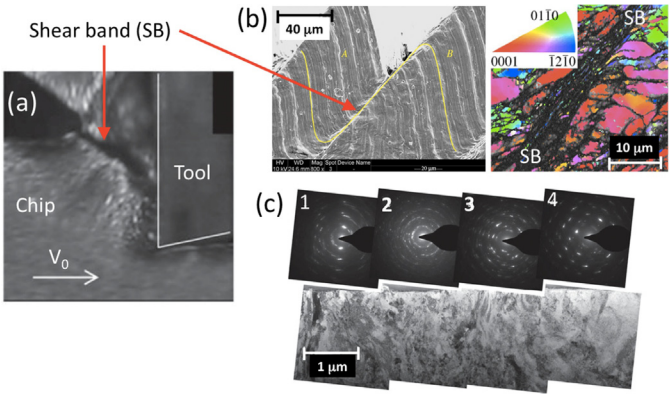

Fig. 31. Shear band characterization in machining using (a) PIV, (b) SEM/EBSD and (c) TEM. The far left panel in (c) represents microstructure in the centre of the shear band [193].

5.3. Microstructure models for machining

Modeling of phase transformations in machining has garnered significant interest due to the emphasis on understanding white layer formation in steels. Multiple works have attempted to model the martensitic transformation by coupling various thermal and thermomechanical models to establish the temperature history of the deformation zone, chip and machined surface. Chou and Evans [58] used a moving heat source model to determine the temperature history of the machined surface as a function of machining parameters, while ignoring strain and strain rate related effects. Umbrello and Filice [220] used FE simulations and empirical relationships for estimating the white layer in machining of AISI 52100. The FE models were coupled with empirical formulations for describing hardness variations for quenching or tempering. The local variations in hardness were estimated using the local temperature history. Ramesh and Melkote [182] developed a FE model that incorporated thermomechanical dependent effects of transformational plasticity and stress/strain-dependent austenite/martensite transformation temperatures.

The effect of microstructure in multi-phase materials has been addressed through multi-constituent FE models that represent individual phases discretely within a single FE mesh. The local morphology for each phase is modelled using elements with differing constitutive properties. Chuzhoy et al. [59] used a multi-constituent FE model to describe microstructure response in orthogonal machining of ductile iron comprised of ferrite and pearlite grains with graphite nodules. The results were similar in

terms of cutting forces and temperatures, as well as the relative morphology of graphite nodules. Further, the resulting stress distributions indicated that the deformation of the pearlite phase contributed more significantly than the ductile iron. This was later expanded upon by Vogler et al. [223] to understand the forces in 3-D micromilling of ductile iron. The results showed that the multi-constituent FE model was able to predict milling forces within 20% of the experimental values.

Prediction of hardening and grain refinement in machining of crystalline materials has included a number of studies that have involved: (1) Zener-Hollomon based frameworks, (2) Johnson-Mehl-Avrami-Kolmogorov (JMAK) kinetics, and (3) continuous dynamic recrystallization models. The first of these are based on empirical characterizations of the effects of strain, strain rate and temperature on recrystallization phenomena in crystalline metals. In this regard, the Zener-Hollomon parameter is given by $Z = \dot{\varepsilon}\, e^{\frac{Q}{RT}}$, where $\dot{\varepsilon}$ is the strain rate, Q is the activation energy, R is the gas constant and T is the temperature. Zener-Hollomon frameworks for predicting the final microstructure generally involve incorporation of the Zener-Hollomon parameter within an FE simulation. In this regard, the FE model is used to determine the locally varying strain, strain rate and temperature distributions during machining and the resulting Zener-Hollomon field is determined. In regions of the material where a threshold strain for recrystallization is achieved, the recrystallized grain size is determined according to an empirical relationship relating initial grain size, the Zener-Hollomon parameter, and material constants. This approach has been utilized by a number of authors, including Caruso et al. [43] for AISI 52100, Pu et al. [179] for MgAZ31B, Rotella and Umbrello [188] for Ti–6Al–4V, M'Saoubi et al. [150] for advanced nickel based superalloys (Inconel 718, Wasapaloy, Udimet 720 and RR1000), Jafarian et al. [119] for Inconel 718, Ambrosy et al. [2] for AISI 4140. As an example, the results for Ti–6Al–4V shown in Fig. 32 indicate that the results match grain size closely with experimental data.

Grain refinement in the deformation zone has also been addressed using modifications of isothermal Johnson-Mehl-Avrami-Kolmogorov (JMAK) kinetics by leveraging similar models utilized for predicting microstructure evolution in metal forming processes. In this regard, the final grain size in the machining process is determined by evaluating the recrystallized volume fraction in the deformed chip and machined surface as a function of time at temperature. The temperature profile is used as an input to determine the final grain size after a threshold strain is achieved. Arisoy and Özel [5] applied this to model microstructure evolution in machining of Ti–6Al–4V. This was followed by the work of Pan et al. [175] who added a phase transformation model according to the time-transformation-temperature profiles for alpha and beta phase titanium. The authors used the model to understand the effect of machining parameters on refinement and phase formation in the machined surface and chip.

Microstructure evolution models based on continuous dynamic recrystallization have also been developed that incorporate well established relations for evaluating evolving dislocation density and

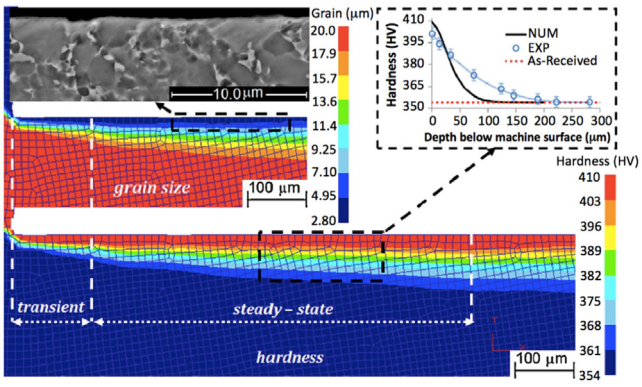

Fig. 32. Subsurface microstructure in machining Ti–6Al–4V [188].

corresponding microstructure refinement (e.g., formation into cell walls and other low energy boundary structures). Ding and Shin [68] incorporated these formulations within an FE model for simulating microstructure evolution in aluminium and copper. The simulation results for dislocation density, grain size and relative grain misorientation were shown to match well with experimental data. Liu et al. [144] provided further capability to also include a grain size evolution law for dynamic recrystallization, wherein the grain size was modelled following a Zener-Hollomon based approach. Further, microstructure evolution was directly coupled with the flow stress model to provide a unified constitutive framework. The model was used to determine effects of parameters on grain size and dislocation density for SS 304 [144] and copper [146], with good agreement with experimental results.

Grain-scale plastic accommodation in macro-scale and micro-scale machining configurations also has been pursued using modeling approaches that have employed crystal plasticity (CP) formulations in describing microstructure response. Zhang et al. [235] modelled the orthogonal cutting of Ti–6Al–4V using discrete cohesive elements to represent the polycrystalline material in the FE framework. In this regard, the deformation of each grain is modelled according to a single crystal wherein specific slip systems are active depending on the loading path. From the results, the authors showed that the CP framework was able to produce accurate estimates of cutting force, as well as to simulate the chip morphology expected for Ti–6Al–4V. Both Zahedi et al. [228] and Tajalli et al. [215] utilized a CP material model to determine the effects of relative orientation of single crystals on chip morphology and machining forces.

An approach to modeling the evolution of crystallographic texture in deformation of a polycrystal is to use a self-consistent modeling framework. The visco-plastic self-consistent (VPSC) approach simulates grain-scale texture evolution by assuming these grains are embedded in a homogeneous equivalent medium (HEM) whose response to deformation is the same as that of the aggregate of the individual grains combined. Basu and Shankar [31] incorporated the VPSC simulation with displacement fields obtained through high speed digital image correlation, as shown in Fig. 33. Good correspondence was found between simulated and experimental textures for machining of copper over a range of rake angles and cutting speeds. Fergani et al. [78] later utilized VPSC with an analytical model of process mechanics to predict texture evolution in machining of AA7075.

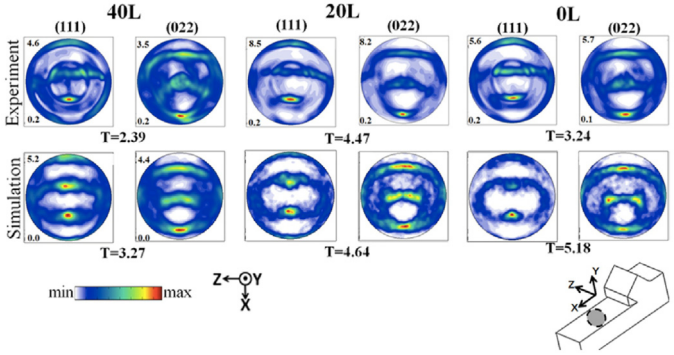

Fig. 33. Experimental and simulated orientation distribution functions for machining of copper [31].

5.4. Future needs and opportunities

1. Integration of microstructure models with commercial software to couple the material response to microstructure evolution.
2. Rigorous examination of microstructure evolution mechanisms in heterogeneous shearing occurring in machining (e.g., laminar flow, shear banding, segmentation).
3. Establishing linkages between heterogeneous material shearing in chip formation and grain-scale plastic accommodation.
4. Development and application of statistical methods for gathering and representing dense microstructure data sets for validation.

6. Conclusions

This keynote paper critically reviewed recent advances in data, models, and experimental techniques to describe the material constitutive properties, tool-workpiece friction, and thermal and microstructure properties needed to model and simulate metal machining. The paper also highlighted the future needs and opportunities in these areas. Future research in these areas will be driven in large part by the industrial need for accurate simulation of machining process performance metrics such as machined surface integrity, including the final microstructure and mechanical properties of the machined part, and tool wear.

Acknowledgements

The authors are grateful to all CIRP members who contributed to the paper. In particular, the authors thank Prof. T.H.C. Childs, Prof. T. Özel, L. Settineri, K. Bouzakis, and Prof. I.S. Jawahir for their inputs. The first author also acknowledges the contributions of Mr. Patxi Fernandez-Zelaia, a doctoral candidate at Georgia Tech.

References

[1] Adibi-Sedeh A, Vaziri M, Pednekar V, Madhavan V, Ivester R (2005) Investigation of the Effect of Using Different Material Models on Finite Element Simulations of Machining. *Proceedings of the 8th CIRP International Workshop on Modelling of Machining Operations*, Chemnitz, Germany, 1–9.

[2] Ambrosy F, Zanger F, Schulze V (2015) Fem-simulation of Machining Induced Nanocrystalline Surface Layers in Steel Surfaces Prepared for Tribological Applications. *CIRP Annals—Manufacturing Technology* 64(1):69–72.

[3] Anderson JT, Saunders OA (1953) Convection from an Isolated Heated Horizontal Cylinder Rotating About its Axis. *Proceedings of the Royal Society of London A: Mathematical Physical and Engineering Sciences* 217(1131):555–562.

[4] Andrade U, Meyers M, Vecchio K, Chokshi A (1994) Dynamic Recrystallization in High-strain, High-strain-rate Plastic Deformation of Copper. *Acta Metallurgica et Materialia* 42(9):3183–3195.

[5] Arisoy Y, Özel T (2015) Prediction of Machining Induced Microstructure in Ti–6Al–4V Alloy Using 3-D FE-Based Simulations: Effects of Tool Micro-geometry, Coating, and Cutting Conditions. *Journal of Materials Processing Technology* 220:1–26.

[6] Arrazola P, Saez-de-Buruaga M, Arrieta I (2006) *Innovative Method Dedicated to the Development of a Ferrite-pearlite Grade Regarding its Machinability*, University of Mondragon, Spain. Internal Report.

[7] Arrazola P, Ugarte D, Dominguez X (2008) A New Approach for the Friction Identification During Machining Through the Use of Finite Element Modeling. *International Journal of Machine Tools and Manufacture* 48(2):173–183.

[8] Arrazola PJ, Özel T (2009) Finite Element Modelling of Machining Processes. *Intelligent Machining: Modelling and Optimization of the Machining Processes and Systems*, Wiley-ISTE.

[9] Arrazola PJ, Özel T (2010) Investigations on the Effects of Friction Modeling in Finite Element Simulation of Machining. *International Journal of Mechanical Sciences* 52(1):31–42.

[10] Arrazola PJ, Özel T, Umbrello D, Davies M, Jawahir IS (2013) Recent Advances in Modelling of Metal Machining Processes. *CIRP Annals* 62(2):695–718.

[11] Astakhov V (2006) *Tribology of Metal Cutting*, Elsevier.

[12] Astakhov V (2013) Tribology of Cutting Tools. *Tribology in Manufacturing Technology*, 1. 1–66.

[13] Astakhov VP (1998) *Metal Cutting Mechanics*, CRC Press, Boca Raton, USA.

[14] Atkins AG (2003) Modelling Metal Cutting Using Modern Ductile Fracture Mechanics: Quantitative Explanations for Some Longstanding Problems. *International Journal of Mechanical Sciences* 45(2):373–396.

[15] Atlati S, Haddag B, Nouari M, Moufki A (2015) Effect of the Local Friction and Contact Nature on the Built-up Edge Formation Process in Machining Ductile Metals. *Tribology International* 90:217–227.

[16] Atlati S, Haddag B, Nouari M, Zenasni M (2014) Thermomechanical Modelling of the Tool–Workmaterial Interface in Machining and its Implementation Using the ABAQUS VUINTER Subroutine. *International Journal of Mechanical Sciences* 87:102–117.

[17] Atmani Z, Haddag B, Nouari M, Zenasni M (2016) Combined Microstructure-based Flow Stress and Grain Size Evolution Models for Multi-physics Modelling of Metal Machining. *International Journal of Mechanical Sciences* 118:77–90.

[18] Attia M, D'Silva N (1983) Thermal Analysis of the Fuel Bearing Pad in the CANDU Reactor—Prediction of Nucleate Boiling. *Proceedings of the 3rd Multiphase Flow and Heat Transfer Symposium*, Florida, USA, 851–863.

[19] Attia MH, Joseph PM, M'Saoubi R (2016) Determination of Convective Heat Transfer from Rotating Workpieces in Dry and Laser-assisted Turning Processes. *Advances in Materials and Processing Technologies* 2(2):324–338.

[20] Attia MH, Kops L (1979) Computer Simulation of Nonlinear Thermoelastic Behavior of a Joint in Machine Tool Structure and its Effect on Thermal Deformation. *Journal of Engineering for Industry* 101(3):355–361.

[21] Attia MH, Kops L (1979) Nonlinear Thermoelastic Behavior of Structural Joints—Solution to a Missing Link for Prediction of Thermal Deformation of Machine Tools. *Journal of Engineering for Industry* 101(3):348–354.

[22] Attia MH, Kops L (1980) Importance of Contact Pressure Distribution on Heat Transfer in Structural Joints of Machine Tools. *Journal of Engineering for Industry* 102(2):159–167.

[23] Attia MH, Kops L (1981) System Approach to the Thermal Behavior and Deformation of Machine Tool Structures in Response to the Effect of Fixed Joints. *Journal of Engineering for Industry* 103(1):67–72.

[24] Attia MH, Kops L (2004) A New Approach to Cutting Temperature Prediction Considering the Thermal Constriction Phenomenon in Multi-Layer Coated Tools. *CIRP Annals—Manufacturing Technology* 53(1):47–52.

[25] Attia MH, Kops L (2004) Thermal Consideration of the Design of Multi-Layer Coated Tools for High Speed Machining. *Proceedings of the ASME International Mechanical Engineering Congress & Exposition*, Anaheim, CA, 803–813.

[26] Bacherla V, Bassani JF (2007) Strain Burst Phenomena in the Necking of a Sheet that Deforms by Non-associated Plastic Flow. *Modelling and Simulation in Materials Science and Engineering* 15(1):S297.

[27] Bai Y, Wierzbicki T (2008) A New Model of Metal Plasticity and Fracture with Pressure and Lode Dependence. *International Journal of Plasticity* 24(6):1071–1096.

[28] Bariani PF, Dal Negro T, Bruschi S (2004) Testing and Modelling of Material Response to Deformation in Bulk Metal Forming. *CIRP Annals—Manufacturing Technology* 53(2):573–595.

[29] Barron RF, Stanley RS (1994) Film Boiling Under an Impinging Cryogenic Jet. *Advances in Cryogenic Engineering* 39:1769–1777.

[30] Basu S, Shankar MR (2014) Spatial Confinement-induced Switchover in Microstructure Evolution During Severe Plastic Deformation at Micrometer Length Scales. *Acta Materialia* 79:146–158.

[31] Basu S, Shankar MR (2015) Crystallographic Textures Resulting from Severe Shear Deformation in Machining. *Metallurgical and Materials Transactions A* 46(2):801–812.

[32] Basu S, Wang Z, Liu R, Saldana C (2016) Enhanced Subsurface Grain Refinement During Transient Shear-based Surface Generation. *Acta Materialia* 116:114–123.

[33] Becker KM (1963) Measurements of Convective Heat Transfer from a Horizontal Cylinder Rotating in a Tank of Water. *International Journal of Heat and Mass Transfer* 6(12):1053–1062.

[34] Bil H, Kilic S, Tekkaya A (2004) A Comparison of Orthogonal Cutting Data from Experiments with Three Different Finite Element Models. *International Journal of Machine Tools & Manufacture* 44:933–944.

[35] Bollig P, Faltin C, Schießl R, Schneider J, Maas U, Schulze V (2015) Considering the Influence of Minimum Quantity Lubrication for Modelling Changes in Temperature, Forces and Phase Transformations During Machining. *Procedia CIRP* 31:142–147.

[36] Bonnet C, Valiorgue E, Rech J, Hamdi H (2008) Improvement of the Numerical Modeling in Orthogonal Dry Cutting of an AISI 316L Stainless Steel by the Introduction of a New Friction Model. *CIRP Journal of Manufacturing Science and Technology* 1(2):114–118.

[37] Brown TL, Saldana C, Murthy TG, Mann JB, Guo Y, Allard LF, King AH, Chandrasekar S (2000) A Study of the Interactive Effects of Strain, Strain Rate and Temperature in Severe Plastic Deformation of Copper. *Acta Materialia* 57:5491–5500.

[38] Buchkremer S, Wu B, Lung D, Münstermann S, Klocke F, Bleck W (2014) FE-Simulation of Machining Processes with a New Material Model. *Journal of Materials Processing Technology* 214(3):599–611.

[39] Burns TJ, Mates SP, Rhorer RL, Whitenton EP, Basak D (2011) Dynamic Properties for Modelling and Simulation of Machining: Effect of Pearlite to Austenite Phase Transition on Flow Stress in AISI 1075 Steel. *Machining Science and Technology* 15:1–20.

[40] Cabanettes F, Rolland J, Dumont F, Rech J, Dimkowski Z (2016) Influence of MQL on Friction at the Tool Workpiece Interface in Machining of an Aluminium Alloy. *Journal of Tribology* 138(2):021107. (10 pp).

[41] Calamaz M, Coupard D, Girot F (2008) A New Material Model for 2D Numerical Simulation of Serrated Chip Formation When Machining Titanium Alloy Ti–6Al–4V. *International Journal of Machine Tools and Manufacture* 48(3–4):275–288.

[42] Calistes R, Swaminathan S, Murthy TG, Huang C, Saldana C, Shankar MR, Chandrasekar S (2009) Controlling Gradation of Surface Strains and Nanostructuring by Large-strain Machining. *Scripta Materialia* 60(1):17–20.

[43] Caruso S, Di Renzo S, Umbrello D, Jayal AD, Dillon OW, Jawahir IS (2011) Finite Element Modeling of Microstructural Changes in Hard Turning. *Advanced Materials Research* 223:960–968.

[44] Cazacu O, Plunkett B, Barlat F (2006) Orthotropic Yield Criterion for Hexagonal Closed Packed Metals. *International Journal of Plasticity* 22(7):1171–1194.

[45] Chaparro B, Thuillier S, Menezes L, Manach P, Fernandes J (2008) Material Parameters Identification: Gradient-based, Genetic and Hybrid Optimization Algorithm. *Computational Materials Science* 44(2):339–346.

[46] Chen S, Kothari J, Tseng AA (1992) Spray and Jet Cooling in Steel Rolling. *International Journal of Heat and Fluid Flow* 13(4):358–369.

[47] Chen SJ, Kothari J, Tseng AA (1991) Cooling of a Moving Plate with an Impinging Circular Water Jet. *Experimental Thermal and Fluid Science* 4(3):343–353.

[48] Childs THC (1973) The Rake Face Action of Cutting Lubricants: An Analysis of and Experiments on the Machining of Iron Lubricated by Carbon Tetrachloride. *Proceedings of the Institution of Mechanical Engineers* 186(1):717–727.

[49] Childs THC (1997) Material Property Requirements for Modelling Metal Machining. *Journal de Physique IV Colloque* 7(C3). C3-XXI-C3-XXXVI.

[50] Childs THC (2006) Friction Modelling in Metal Cutting. *Wear* 260:310–318.

[51] Childs THC (2006) Numerical Experiments on the Influence of Material and Other Variables on Plane Strain Continuous Chip Formation in Metal Machining. *International Journal of Mechanical Sciences* 48:307–322.

[52] Childs THC (2009) Modelling Orthogonal Machining of Carbon Steels. Part I: Strain Hardening and Yield Delay Effects. *International Journal of Mechanical Sciences* 51:402–411.

[53] Childs THC (2010) Surface Energy, Cutting Edge Radius and Material Flow Stress Size Effects in Continuous Chip Formation of Metals. *CIRP Journal of Manufacturing Science and Technology* 3:27–39.

[54] Childs THC, Maekawa K, Maulik P (1988) Effects of Coolant on Temperature Distribution in Metal Machining. *Materials Science and Technology* 4 (11):1006–1019.

[55] Childs THC, Maekawa K, Obikawa T, Yamane Y (2000) *Metal Machining: Theory and Applications*, Elsevier, Oxford, U.K.

[56] Childs THC, Rahmad R (2009) Modelling Orthogonal Machining of Carbon Steels. Part II: Comparisons with Experiments. *International Journal of Mechanical Sciences* 51:465–472.

[57] Childs THC, Rahmad R (2010) Modifying Strain-hardening of Carbon Steels for Improved Finite Element Simulation of Orthogonal Machining. *Proceedings of the Institution of Mechanical Engineers Part B: Journal of Engineering Manufacture* 54:721–731.

[58] Chou YK, Evans CJ (1999) White Layers and Thermal Modeling of Hard Turned Surfaces. *International Journal of Machine Tools and Manufacture* 39(12):1863–1881.

[59] Chuzhoy L, DeVor RE, Kapoor SG, Bammann G (2002) Microstructure-level Modeling of Ductile Iron Machining. *Journal of Manufacturing Science and Engineering* 124(2):162–169.

[60] Claudin C, Mondelin A, Rech J, Fromentin G (2010) Effects of a Straight Oil on Friction at the Tool-work Material Interface in Machining. *International Journal of Machine Tools and Manufacture* 50:681–688.

[61] Collier JG, Thome JR (1994) *Convective Boiling and Condensation*, 3rd ed. Clarendon Press, Oxford, U.K.

[62] Courbon C, Mabrouki T, Rech J, Mazuyer D, D'Eramo E (2011) New Thermal Issues on the Modelling of Tool-workpiece Interaction: Application to Dry Cutting of AISI 1045 Steel. *Advanced Materials Research* 223:286–295.

[63] Courbon C, Mabrouki T, Rech J, Mazuyer D, D'Eramo E (2013) On the Existence of a Thermal Contact Resistance at the Tool-chip Interface in Dry Cutting of AISI 1045: Formation Mechanisms and Influence on the Cutting Process. *Applied Thermal Engineering* 50(1):1311–1325.

[64] Courbon C, Mabrouki T, Rech J, Mazuyer D, Perrard F, D'Eramo E (2013) Towards a Physical FE Modelling of a Dry Cutting Operation: Influence of Dynamic Recrystallization When Machining AISI 1045. *Procedia CIRP* 8:516–521.

[65] Davies MA, Ueda T, M'Saoubi R, Mullany B, Cooke AL (2007) On the Measurement of Temperature in Material Removal Processes. *CIRP Annals—Manufacturing Technology* 56(2):581–604.

[66] Denguir LA, Outeiro JC, Fromentin G, Vignal V, Besnard R (2016) Orthogonal Cutting Simulation of OFHC Copper Using a New Constitutive Model Considering the State of Stress and the Microstructure Effects. *Procedia CIRP* 46:238–241.

[67] Dhir VK (1991) Nucleate and Transition Boiling Heat Transfer under Pool and External Flow Conditions. *International Journal of Heat and Fluid Flow* 12 (4):290–314.

[68] Ding H, Shin Y (2011) Modeling of Grain Refinement in Aluminum and Copper Subjected to Cutting. *Computational Materials Science* 50:3016–3025.

[69] Ding H, Shin Y (2014) Dislocation Density-based Grain Refinement Modeling of Orthogonal Cutting of Titanium. *Journal of Manufacturing Science and Engineering* 136. 041003–1 (11pp).

[70] Dreitser GA (2003) Modern Problems of Cryogenic Heat Transfer and its Enhancement (Generalization of Experimental Results, Practical Recommendations and Different Applications). Kakac S, et al. (Eds.) *Low Temperature and Cryogenic Refrigeration*, 99. Springer Netherlands, Dordrecht 201–220.

[71] Dropkin D, Carmi A (1957) Natural Convection Heat Transfer from a Horizontal Cylinder Rotating in Air. *Transactions of ASME* 79(4):741–749.

[72] Elsayed A, Attia MH, Damir A (2016) *Computer Fluid Dynamics Analysis for Enhanced Cooling of Cutting Tools in Turning Operation. Internal Report, Structures, Materials and Manufacturing Laboratory*, National Research Council of Canada (NRC).

[73] Elshwain AEI, Redzuan N, Yusof NM (2013) Machinability of Nickel and Titanium Alloys Under of Gas-based Coolant-lubricants (Cls)—A Review. *International Journal of Research in Engineering and Technology* 2(11):690–702.

[74] Estrin Y, Toth L, Molinari A, Brechet Y (1998) A Dislocation Based Model for All Hardening Stages in Large Strain Deformation. *Acta Materialia* 46:5509–5522.

[75] Etemad A (1955) Free Convection Heat Transfer from a Rotating Cylinder to Ambient Air with Interferometric Study of Flow. *Transactions of ASME* 77:1283–1289.

[76] Fahad M, Mativenga PT, Sheikh MA (2011) An Investigation of Multilayer Coated (TiCN/Al_2O_3-TIN) Tungsten Carbide Tools in High Speed Cutting Using a Hybrid Finite Element and Experimental Technique. *Proceedings of the Institution of Mechanical Engineers Part B: Journal of Engineering Manufacture* 225(10):1835–1850.

[77] Faverjon P, Rech J, Leroy R (2013) Influence of Minimum Quantity Lubrication on Friction Coefficient and Work-material Adhesion during Machining of Cast Aluminium with Various Cutting Tool Substrates Made of PCD, HSS and Carbides. *Journal of Tribology* 135(4):041602. (8 pages).

[78] Fergani O, Tabei A, Garmestani H, Liang SY (2014) Prediction of Polycrystalline Materials Texture Evolution in Machining via Viscoplastic Self-consistent Modeling. *Journal of Manufacturing Processes* 16(4):543–550.

[79] Field J, Walley S, Proud W, Goldrein H, Siviour C (2004) Review of Experimental Techniques for High Rate Deformation and Shock Studies. *International Journal of Impact Engineering* 30:725–775.

[80] Filice L, Micari F, Rizzuti S, Umbrello D (2007) A Critical Analysis on the Friction Modelling in Orthogonal Machining. *International Journal of Machine Tools & Manufacture* 47:709–714.

[81] Filice L, Micari F, Rizzuti S, Umbrello D (2008) Dependence of Machining Simulation Effectiveness on Material and Friction Modelling. *Machining Science and Technology* 12(3):370–389.

[82] Filice L, Umbrello D, Micari F, Settineri L (2007) On the Finite Element Simulation of Thermal Phenomena in Machining Processes. *Advanced Methods in Material Forming*, Springer, Berlin Heidelberg263–278.

[83] Fitzer E (1967) *Thermophysical Properties of Materials. DTIC Document*.

[84] Follansbee P, Kocks U (1988) A Constitutive Description of the Deformation of Copper Based on the Use of the Mechanical Threshold Stress as an Internal State Variable. *Scripta Metallurgica Materialia* 36:81–93.

[85] Germain G, Morel A, Braham-Bouchnak T (2013) Identification of Material Constitutive Laws Representative of Machining Conditions for Two Titanium Alloys: Ti6Al4V and Ti555-3. *Journal of Engineering Materials and Technology* 135(3):031002. (11 pp).

[86] Giannuzzi L, Stevie F (1999) A Review of Focused Ion Beam Milling Techniques for TEM Specimen Preparation. *Micron* 30(3):197–204.

[87] Goldstein RJ, Franchett ME (1988) Heat Transfer from a Flat Surface to an Oblique Impinging Jet. *Journal of Heat Transfer* 110(1):84–90.

[88] Grimvall G (1999) *Thermophysical Properties of Materials*, Elsevier.

[89] Grzesik W (1999) Experimental Investigation of the Cutting Temperature When Turning with Coated Indexable Inserts. *International Journal of Machine Tools and Manufacture* 39(3):355–369.

[90] Grzesik W (1999) Experimental Investigation of the Influence of Adhesion on the Frictional Conditions in the Cutting Process. *Tribology International* 33:131–140.

[91] Grzesik W (2000) The Influence of Thin Hard Coatings on Frictional Behaviour in the Orthogonal Cutting Process. *Tribology International* 33(2):131–140.

[92] Grzesik W (2008) *Advanced Machining Processes of Metallic Materials*, Elsevier.

[93] Grzesik W, Denkena B, Zak K, Grove T, Bergman B (2015) Correlation between Friction and Wear of Cubic Boron Nitride Cutting Tools in Precision Hard Machining. *Journal of Manufacturing Science and Engineering* 138(3):031010. (6 pages).

[94] Grzesik W, Denkena B, Zak K, Grove T, Bergman B (2016) Energy Consumption Characterization in Precision Hard Machining Using CBN Cutting Tool. *International Journal of Advanced Manufacturing Technology* 85(9):2839–2845.

[95] Grzesik W, Nielsony P (2004) Prediction of Friction and Heat Flow in Machining Incorporating Thermophysical Properties of the Coating-chip Interface. *Wear* 256:108–117.

[96] Grzesik W, Nielsony P (2003) Thermophysical-property-based Selection of Tool Protective Coatings for Dry Machining of Steels. *Journal of Manufacturing Science and Engineering* 125(4):689–695.

[97] Grzesik W, Nielsony P (2004) Physics Based Modelling of Interface Temperatures in Machining with Multilayer Coated Tools at Moderate Cutting Speeds. *International Journal of Machine Tools and Manufacture* 44(9):889–901.

[98] Grzesik W, Rech J, Zak K (2014) Determination of Friction in Metal Cutting With Tool Wear and Flank Face Effects. *Wear* 317:8–10.

[99] Grzesik W, van Luttervelt C (2001) An Investigation of the Thermal Effects in Orthogonal Cutting Associated with Multilayer Coatings. *CIRP Annals—Manufacturing Technology* 50(1):53–56.

[100] Grzesik W, Zak K (2013) Friction Quantification in the Oblique Cutting With CBN Chamfered Tools. *Wear* 304:36–42.

[101] Gulati P, Katti V, Prabhu SV (2009) Influence of the Shape of the Nozzle on Local Heat Transfer Distribution Between Smooth Flat Surface and Impinging Air Jet. *International Journal of Thermal Sciences* 48(3):602–617.

[102] Guo Y, Saldana C, Compton WD, Chandrasekar S (2011) Controlling Deformation and Microstructure on Machined Surfaces. *Acta Materialia* 59(11):4538–4547.

[103] Guo YB, Wen Q, Woodbury KA (2006) Dynamic Material Behavior Modeling Using Internal State Variable Plasticity and its Application in Hard Machining Simulations. *Journal of Manufacturing Science and Engineering* 128:749–759.

[104] Hadad M, Sadeghi B (2012) Thermal Analysis of Minimum Quantity Lubrication-MQL Grinding Process. *International Journal of Machine Tools and Manufacture* 63:1–15.

[105] Hadad MJ, Tawakoli T, Sadeghi MH, Sadeghi B (2012) Temperature and Energy Partition in Minimum Quantity Lubrication—MQL Grinding Process. *International Journal of Machine Tools and Manufacture* 54–55:10–17.

[106] Haglund A, Kishawy H, Rogers R (2008) An Exploration of Friction Models for the Chip-tool Interface using an Arbitrary Lagrangian–Eulerian Finite Element Model. *Wear* 265(3–4):452–460.

[107] Hamann J, Meslin F, Sartkulvanich J (2002) Criteria for the Quality Assessment of Constitutive Equations Dedicated to Metal Cutting Models. *Machining Science and Technology* 6(3):331–351.

[108] Hedenquist P, Olsson M (1991) Sliding Wear Testing of Coated Cutting Tool Materials. *Tribology International* 23(3):143–150.

[109] Ho CY, Powell RW, Liley PE (1974) *Thermal Conductivity of the Elements: A Comprehensive Review*, Published by the American Chemical Society for the National Bureau of Standards.

[110] Holmberg K, Matthews A (1998) *Properties, Techniques and Applications in Surface Engineering, Coating Tribology*, Elsevier, Amsterdam.

[111] Holmquist T, Johnson G (1991) Determination of Constants and Comparison of Results for Various Constitutive Models. *Journal de Physique IV Colloque* 1(C3). C3-853-C3-860.

[112] Hor A, Morel F, Lebrun JL, Germain G (2013) Modelling, Identification and Application of Phenomenological Constitutive Laws Over a Large Strain Rate and Temperature Range. *Mechanics of Materials* 64:91–110.

[113] Huang C, Murthy TG, Shankar MR, M'Saoubi R, Chandrasekar S (2008) Temperature Rise in Severe Plastic Deformation of Titanium at Small Strain-rates. *Scripta Materialia* 58(8):663–666.

[114] Hughes D, Hansen N (1997) High Angle Boundaries Formed by Grain Subdivision Mechanisms. *Acta Materialia* 45(9):3871–3886.

[115] Hutchings IM (1992) *Tribology. Friction and Wear of Engineering Materials*, Edward Arnold, London.

[116] Itoigawa F, Takeuchi D, Nakamura T, Childs THC (2007) Experimental Study of Lubrication Mechanism in MQL Intermittent Cutting Process. *Machining Science and Technology* 11(3):355–365.

[117] Ivester R, Whitenton E, Deshayes L (2005) Comparison of Measurements and Simulation for Machining of Aluminum. *Transactions of the North American Manufacturing Research Institution of SME* 33:429–436.

[118] Iwata K, Osakada K, Teresaka X (1984) Process Modeling of Orthogonal Cutting by the Rigid-plastic Finite Element Method. *Journal of Materials Processing Technology* 106:132–138.

[119] Jafarian F, Ciaran MI, Umbrello D, Arrazola P, Filice L, Amirabadi H (2014) Finite Element Simulation of Machining Inconel 718 Alloy Including Microstructure Changes. *International Journal of Mechanical Sciences* 88:110–121.

[120] Jambunathan K, Lai E, Moss MA, Button BL (1992) A Review of Heat Transfer Data for Single Circular Jet Impingement. *International Journal of Heat and Fluid Flow* 13(2):106–115.

[121] Jaspers SPFC, Dautzenberg JH (2002) Material Behaviour in Conditions Similar to Metal Cutting: Flow Stress in the Primary Shear Zone. *Journal of Materials Processing Technology* 122(2–3):322–330.

[122] Jawahir IS, Attia MH, Biermann D, Duflou J, Klocke F, Meyer D, Newman ST, Pusavec F, Putz M, Rech J, Schulze V, Umbrello D (2016) Cryogenic Manufacturing Processes. *CIRP Annals—Manufacturing Technology* 65(2):713–736.

[123] Jawahir IS, Brinksmeier E, M'Saoubi R, Aspinwall DK, Outeiro JC, Meyer D, Umbrello D, Jayal AD (2011) Surface Integrity in Material Removal Processes: Recent Advances. *CIRP Annals—Manufacturing Technology* 60(2):603–626.

[124] Jiang L, Roos A, Liu P (1997) The Influence of Austenite Grain Size and its Distribution on Chip Deformation and Tool Life During Machining of AISI 304L. *Metallurgical and Materials Transactions A* 28(11):2415–2422.

[125] Jin T, Stephenson DJ, Rowe WB (2003) Estimation of the Convection Heat Transfer Coefficient of Coolant within the Grinding Zone. *Proceedings of the Institution of Mechanical Engineers Part B: Journal of Engineering Manufacture* 217(3):397–407.

[126] Johnson GR, Cook WH (1983) A Constitutive Model and Data for Metals Subjected to High Strains, High Strain Rates, and High Temperatures. *Proceedings of the 7th International Symposium on Ballistics*, Hague, Netherlands, 541–547.

[127] Johnson GR, Cook WH (1985) Fracture Characteristics of Three Metals Subjected to Various Strains, Strain Rates, Temperatures and Pressures. *Engineering Fracture Mechanics* 21(1):31–48.

[128] Joseph PM, Attia MH, Shi B (2016) *Experimental and Numerical Analysis of Heat Transfer in CVD Coated Carbide Tools. Internal Report SMM-TR-MR-2016-01*, National Research Council, Canada.

[129] Kim NK, Guo C, Malkin S (1997) Heat Flux Distribution and Energy Partition in Creep-feed Grinding. *CIRP Annals— Manufacturing Technology* 46(1):227–232.

[130] Klocke F, Krieg T (1999) Coated Tools for Metal Cutting—Features and Applications. *CIRP Annals—Manufacturing Technology* 48(2):515–525.

[131] Kolsky H (1949) An Investigation of the Mechanical Properties of Materials at Very High Loading Rates. *Proceedings of the Physical Society B* 62(11):676–700.

[132] Komanduri R (1982) Some Clarifications on the Mechanics of Chip Formation When Machining Titanium Alloys. *Wear* 76(1):15–34.

[133] König W, Fritsch R, Kammermeier D (1992) New Approaches to Characterizing the Performance of Coated Cutting Tools. *CIRP Annals—Manufacturing Technology* 41(1):49–54.

[134] Kopalinsky E, Oxley P (1995) Explaining the Mechanics of Metallic Sliding Friction and Wear in Terms of Slipline Field Models of Asperity Deformation. *Wear* 190(2):145–154.

[135] Kops L, Arenson M (1999) Determination of Convective Cooling Conditions in Turning. *CIRP Annals—Manufacturing Technology* 48(1):47–52.

[136] Kragelsky I, Dobytchin M, Kombalov V (1975) *Friction and Wear: Calculation Methods*. Pergamon: Oxford.

[137] Kuhn H, Medlin D (2000) *ASM Handbook: Mechanical Testing and Evaluation Vol. 8*, ASM International, Materials Park, Ohio.

[138] Lee J, Lee SJ (2000) The Effect of Nozzle Aspect Ratio on Stagnation Region Heat Transfer Characteristics of Elliptic Impinging Jet. *International Journal of Heat and Mass Transfer* 43(4):555–575.

[139] Lee S, Hwang J, Shankar M, Chandrasekar S (2006) Large Strain Deformation Field in Machining. *Metallurgical and Materials Transactions A* 375(5):1633–1643.

[140] Leseur DR (2000) *Experimental Investigations of Material Models for Ti–6Al–4V Titanium and 2024-T3 Aluminum. Lawrence Livermore National Laboratory Final Report DOT/FAA/AR-00/25*.

[141] Li X (1996) Study of the Jet-Flow Rate of Cooling in Machining Part 1. Theoretical Analysis. *Journal of Materials Processing Technology* 62(1–3):149–156.

[142] Li X (1996) Study of the Jet-flow Rate of Cooling in Machining Part 2. Simulation Study. *Journal of Materials Processing Technology* 62(1–3):157–165.

[143] Liu R, Melkote SN, Morehouse J, Pucha R, Man X, Marusich T (2013) An Enhanced Constitutive Material Model for Machining of Ti–6Al–4V Alloy. *Journal of Materials Processing Technology* 213:2238–2246.

[144] Liu R, Salahshoor M, Melkote S, Marusich T (2014) A Unified Internal State Variable Material Model for Inelastic Deformation and Microstructure Evolution in SS304. *Materials Science and Engineering A* 594:352–363.

[145] Liu R, Salahshoor M, Melkote SN, Marusich T (2014) The Prediction of Machined Surface Hardness Using a New Physics-based Material Model. *Procedia CIRP* 13:249–256.

[146] Liu R, Salahshoor M, Melkote SN, Subramaniam J, Marusich T (2014) A Unified Material Model Including Dislocation Drag and its Application to Simulation of Orthogonal Cutting of OFHC Copper. *Journal of Materials Processing Technology* 216:328–338.

[147] Liu X, Lienhard VJH, Lombara JS (1991) Convective Heat Transfer by Impingement of Circular Liquid Jets. *Journal of Heat Transfer* 113(3):571–582.

[148] Lu T (2014) *A Metrics-based Sustainability Assessment of Cryogenic Machining Using Modeling and Optimization of Process Performance. Ph.D, Thesis*, University of Kentucky.

[149] Luo J, Li M, Yu W, Li H (2010) The Variation of Strain Rate Sensitivity Exponent and Strain Hardening Exponent in Isothermal Compression of Ti–6Al–4V Alloy. *Materials & Design* 31(2):741–748.

[150] M'Saoubi R, Axinte D, Herbert C, Hardy M, Salmon P (2014) Surface Integrity of Nickel-based Alloys Subjected to Severe Plastic Deformation by Abusive Drilling. *CIRP Annals—Manufacturing Technology* 63(1):61–64.

[151] M'Saoubi R, Chandrasekaran H (2005) Innovative Methods for the Investigation of Tool-chip Adhesion and Layer Formation During Machining. *CIRP Annals—Manufacturing Technology* 54(1):59–62.

[152] M'Saoubi R, Ryde L (2005) Application of the EBSD Technique for the Characterisation of Deformation Zones in Metal Cutting. *Materials Science and Engineering: A* 405(1):339–349.

[153] Ma G, Wang L, Gao H, Ahang J, Reddyhoff T (2015) The Friction Coefficient Evolution of a Tin Coated Contact During Sliding Wear. *Applied Surface Science* 345:109–115.

[154] Maekawa K, Shirakashi T, Usui E (1983) Flow Stress of Low Carbon Steel at High Temperature and Strain Rate (Part 2)—Flow Stress Under Variable Temperature and Variable Strain Rate. *Bulletin of the Japan Society of Precision Engineering* 17(3):167–172.

[155] Maglic KD, Cezairliyan A, Peletsky VE (1984) *Compendium of Thermophysical Property Measurement Methods: Vol. 1, Survey of Measurement Techniques*, Plenum Press, New York, NY.

[156] Man X, Ren D, Usui S, Johnson C, Marusich T (2012) Validation of Finite Element Cutting Force Prediction for End Milling. *Procedia CIRP* 663–668.

[157] Martin M, Shen T, Thadhani N (2008) Instrumented Anvil-on-rod Impact Experiments for Validating Constitutive Strength Model for Simulating Transient Dynamic Deformation Response of Metals. *Materials Science and Engineering A* 494:416–424.

[158] Mecking H, Kocks UF (1981) Kinetics of Flow and Strain-hardening. *Acta Metallurgica* 29(11):1865–1875.

[159] Melkote SN, Liu R, Fernandez-Zelaia P, Marusich T (2015) A Physically-based Constitutive Model for Simulation of Segmented Chip Formation in Orthogonal Cutting of Commercially-pure Titanium. *CIRP Annals—Manufacturing Technology* 64(1):65–68.

[160] Minnaar K, Zhou M (1998) An Analysis of the Dynamic Shear Failure Resistance of Structural Metals. *Journal of Mechanics of Physics and Solids* 46 (10):2155–2170.

[161] Mohan VS, Balaji AK (2002) On Modeling the Tool-chip Contact in Machining of Plain Carbon Steels with Multi-layer Coated Cutting Tools. *Proceedings of the 5th CIRP International Workshop on Modeling of Machining Operations* 109–121.

[162] Moufki A, Molinari A, Dudzinski D (1998) Modelling of Orthogonal Cutting with a Temperature Dependent Friction Law. *Journal of Mechanics and Physics of Solids* 46(10):2103–2138.

[163] Nemat-Nasser S, Issacs J, Starrett J (1991) Hopkinson Techniques for Dynamic Recovery Experiments. *Proceedings of the Physical Society A* 435:371–391.

[164] Neugebauer R, Bouzakis K, Denkena B, Klocke F, Sterzing A, Tekkaya AE, Wertheim R (2011) Velocity Effects in Metal Forming and Machining Processes. *CIRP Annals—Manufacturing Technology* 60(1):627–650.

[165] O'Donovan TS, Murray DB (2007) Jet Impingement Heat Transfer—Part I: Mean and Root-Mean-square Heat Transfer and Velocity Distributions. *International Journal of Heat and Mass Transfer* 50(17–18):3291–3301.

[166] Olsson M, Soderberg S, Jacobson S, Hogmark S (1989) Simulation of Cutting Tool Wear by a Modified Pin-on-disc Test. *International Journal of Machine Tools and Manufacture* 29(3):377–390.

[167] Outeiro JC, Campocasso S, Denguir LA, Fromentin G, Vignal V, Poulachon G (2015) Experimental and Numerical Assessment of Subsurface Plastic Deformation Induced by OFHC Copper Machining. *CIRP Annals—Manufacturing Technology* 64(1):53–56.

[168] Outeiro JC, Umbrello D, M'Saoubi R (2006) Experimental and Numerical Modelling of the Residual Stresses Induced in Orthogonal Cutting of AISI 316L Steel. *International Journal of Machine Tools and Manufacture* 46(14):1786–1794.

[169] Outeiro JC, Umbrello D, M'Saoubi R, Jawahir IS (2015) Evaluation of Present Numerical Models for Predicting Metal Cutting Performance and Residual Stresses. *Machining Science and Technology* 19(2):183–216.

[170] Özel T (2006) The Influence of Friction Models on Finite Element Simulations of Machining. *International Journal of Machine Tools & Manufacture* 46(5):518–530.

[171] Özel T, Karpat Y (2007) Identification of Constitutive Material Model Parameters for High Strain Rate Metal Cutting Conditions Using Evolutionary Computational Algorithms. *Materials and Manufacturing Processes* 22(5):659–667.

[172] Özel T, Zeren E (2004) Determination of Work Material Flow Stress and Friction for FEA of Machining Using Orthogonal Cutting Tests. *Journal of Materials Processing Technology* 153–154:1019–1025.

[173] Özerdem B (2000) Measurement of Convective Heat Transfer Coefficient for a Horizontal Cylinder Rotating in Quiescent Air. *International Communications in Heat and Mass Transfer* 27(3):389–395.

[174] Özlü E, Budak E, Molinari A (2009) Analytical and Experimental Investigation of Rake Contact and Friction Behavior in Metal Cutting. *International Journal of Machine Tools & Manufacture* 49(11):865–875.

[175] Pan Z, Liang SY, Garmestani H, Shih DS (2016) Prediction of Machining-induced Phase Transformation and Grain Growth of Ti–6Al–4V Alloy. *The International Journal of Advanced Manufacturing Technology* 87(1):859–866.

[176] Parker WJ, Jenkins RJ, Butler CP, Abbott GL (1961) Flash Method of Determining Thermal Diffusivity, Heat Capacity, and Thermal Conductivity. *Journal of Applied Physics* 32(9):1679–1684.

[177] Perring L, Kuntz JJ, Bussy F, Gachon JC (2001) Heat Capacity Measurements by Differential Scanning Calorimetry in the Pd–Pb, Pd–Sn and Pd–In Systems. *Thermochimica Acta* 366(1):31–36.

[178] Powell RW, Ho CY, Liley PE (1966) *Thermal Conductivity of Selected Materials*, U.S. Dept. of Commerce, National Bureau of Standards; for sale by the Superintendent of Documents U.S. Govt. Print. Off.

[179] Pu Z, Yang S, Song GL, Dillon O, Puleo D, Jawahir IS (2011) Ultrafine-Grained Surface Layer on Mg–Al–Zn Alloy Produced by Cryogenic Burnishing for Enhanced Corrosion Resistance. *Scripta Materialia* 65(6):520–523.

[180] Puls H, Klocke F, Lung D (2012) A New Experimental Methodology to Analyse the Friction Behaviour at the Tool-chip Interface in Metal Cutting. *Production Engineering* 1–6.

[181] Puls H, Klocke F, Lung D (2014) Experimental Investigation on Friction under Metal Cutting Conditions. *Wear* 310:63–71.

[182] Ramesh A, Melkote SN (2008) Modeling of White Layer Formation Under Thermally Dominant Conditions in Orthogonal Machining of Hardened AISI 52100 Steel. *International Journal of Machine Tools and Manufacture* 48 (3):402–414.

[183] Rao VV, Trass O (1964) Mass Transfer from a Flat Surface to an Impinging Turbulent Jet. *The Canadian Journal of Chemical Engineering* 42(3): 95–99.

[184] Rech J, Arrazola P, Claudin C, Courbon C, Pusavec F, Kopac J (2013) Characterization of Friction and Heat Partition Coefficients at the Tool-work Material Interface in Cutting. *CIRP Annals—Manufacturing Technology* 61(1): 79–82.

[185] Rech J, Claudin C, Grzesik W, Zalisz Z (2008) Characterization of the Friction Properties of Various Coatings at the Tool-chip-workpiece Interfaces in Dry Machining of AISI 4140 Steel. *Proceedings of the Institution of Mechanical Engineers Part J: Journal of Engineering Tribology* 222:617–627.

[186] Rech J, Kusiak A, Battaglia JL (2004) Tribological and Thermal Functions of Cutting Tool Coatings. *Surface and Coatings Technology* 186(3):364–371.

[187] Rhim SH, Oh SI (2006) Prediction of Serrated Chip Formation in Metal Cutting Process with New Flow Stress Model for AISI 1045 Steel. *Journal of Materials Processing Technology* 161:417–422.

[188] Rotella G, Umbrello D (2014) Finite Element Modeling of Microstructural Changes in Dry and Cryogenic Cutting of Ti6Al4V Alloy. *CIRP Annals—Manufacturing Technology* 63(1):69–72.

[189] Rowe WB (2001) Thermal Analysis of High Efficiency Deep Grinding. *International Journal of Machine Tools and Manufacture* 41(1):1–19.

[190] Sadek A, Attia MH, Meshreki M, Shi B (2013) Characterization and Optimization of Vibration—Assisted Drilling of Fibre Reinforced Epoxy Laminates. *CIRP Annals—Manufacturing Technology* 62(1):91–94.

[191] Sadek A, Meshreki M, Attia MH (2012) Characterization and Optimization of Orbital Drilling of Woven Carbon Fiber Reinforced Epoxy Laminates. *CIRP Annal—Manufacturing Technology* 61(1):123–126.

[192] Sagapuram D, Efe M, Moscoso W, Chandrasekar S, Trumble KP (2013) Controlling Texture in Magnesium Alloy Sheet by Shear-based Deformation Processing. *Acta Materialia* 61(18):6843–6856.

[193] Sagapuram D, Viswanathan K, Mahato A, Sundaram NK, M'Saoubi R, Trumble KP, Chandrasekar S (2016) Geometric Flow Control of Shear Bands by Suppression of Viscous Sliding. *Proceedings of the Royal Society A* 472 (2192):20160167.

[194] Sagapuram D, Yueng H, Guo Y, Mahato A, M'Saoubi R, Compton WD, Trumble KP, Chandrasekar S (2015) On Control of Flow Instabilities in Cutting of Metals. *CIRP Annals—Manufacturing Technology* 64(1):49–52.

[195] Sagot B, Antonini G, Christgen A, Buron F (2008) Jet Impingement Heat Transfer on a Flat Plate at a Constant Wall Temperature. *International Journal of Thermal Sciences* 47(12):1610–1619.

[196] Saldana C, King AH, Chandrasekar S (2012) Thermal Stability and Strength of Deformation Microstructures in Pure Copper. *Acta Materialia* 60(10):4107–4116.

[197] San-Juan M, Martin O, Santos F (2010) Experimental Study of Friction from Cutting Forces in Orthogonal Milling. *International Journal of Machine Tools and Manufacture* 50(7):591–600.

[198] Schankula MH, Patterson DW, Yovanovich MM (1983) The Effect of Oxide Films on the Thermal Resistance Between Contacting Zirconium Alloys. *Materials in Nuclear Energy*, ASM, Ohio106–111.

[199] Schulze V, Michna J, Schneider J, Gumhsch P (2011) Modelling of Cutting Induced Surface Phase Transformations Considering Friction Effects. *Procedia Engineering* 19:331–336.

[200] Schulze V, Michna J, Zanger F, Faltin C, Maas U, Schneider J (2013) Influence of Cutting Parameters, Tool Coatings and Friction on the Process Heat in Cutting Processes and Phase Transformations in Workpiece Surface Layers. *HTM Journal of Heat Treatment and Materials* 68:22–31.

[201] Semiatin SL, Bieler TR (2001) The Effect of Alpha-platelet Thickness on Plastic Flow During Hot Working of Ti–6Al–4V with a Transformed Microstructure. *Acta Materialia* 49(17):3565–3573.

[202] Settineri L (2005) Surface Properties and Performance of Multilayer Coated Tools in Turning Inconel. *CIRP Annals—Manufacturing Technology* 54(1):515–518.

[203] Settineri L, Faga M (2008) Nanostructured Cutting Tools Coatings for Machining of Titanium. *Machining Science and Technology* 12(2):158–169.

[204] Shankar MR, Rao BC, Lee S, Chandrasekar S, King AH, Compton WD (2006) Severe Plastic Deformation (SPD) of Titanium at Near-ambient Temperature. *Acta Materialia* 54(14):3691–3700.

[205] Shankar MR, Verma R, Rao BC, Chandrasekar S, Compton WD, King AH, Trumble KP (2007) Severe Plastic Deformation of Difficult-to-deform Materials at Near-ambient Temperatures. *Metallurgical and Materials Transactions A* 38A:1899–1905.

[206] Shao Y, Li B, Chiang KN, Liang SY (2015) Physics-based Analysis of Minimum Quantity Lubrication Grinding. *International Journal of Advanced Manufacturing Technology* 79(9):1659–1670.

[207] Shaw MC (2005) *Metal Cutting Principles*, 2nd ed. Oxford University Press, Oxford.

[208] Shi G, Deng X, Shet C (2002) A Finite Element Study of the Effect of Friction in Orthogonal Metal Cutting. *Finite Elements in Analysis and Design* 38(9):863–883.

[209] Shi J, Liu CR (2004) The Influence of Material Models on Finite Element Simulation of Machining. *Journal of Manufacturing Science and Engineering* 126:849–857.

[210] Shirakashi T, Usui E (1973) Friction Characteristics on Tool Face in Metal Machining. *Journal of the Japanese Society of Precision Engineering* 39:966–972.

[211] Sima M, Özel T (2010) Modified Material Constitutive Models for Serrated Chip Formation Simulations and Experimental Validation in Machining of Titanium Alloy Ti–6Al–4ÖV. *International Journal of Machine Tools and Manufacture* 50(11):943–960.

[212] Smolenicki D, Boos J, Kuster F, Roefolds H, Wyen C (2014) In-process Measurement of Friction Coefficient in Orthogonal Cutting. *CIRP Annals—Manufacturing Technology* 60(1):97–100.

[213] Suh N, Sin H (1981) The Genesis of Friction. *Wear* 69:91–114.

[214] Svoboda A, Wedberg D, Lindgren LE (2010) Simulation of Metal Cutting Using a Physically Based Plasticity Model. *Modelling and Simulation in Materials Science and Engineering* 18:075005. (19pp).

[215] Tajalli S, Movahhedy M, Akbari J (2014) Simulation of Orthogonal Microcutting of FCC Materials Based On Rate-dependent Crystal Plasticity Finite Element Model. *Computational Materials Science* 86:79–87.

[216] Touloukian Y, Kirby R, Taylor E, Lee T (1977) Thermophysical Properties of Matter—The TPRC Data Series. Thermal Expansion—Nonmetallic Solids, Volume 13. Lafayette. *Thermophysical and Electronic Properties Information Analysis Center*, .

[217] Touloukian YS, Powell RW, Ho CY, Nicolaou MC (1974) *Thermophysical Properties of Matter—The TPRC Data Series. Volume 10. Thermal Diffusivity (Data book)*, IFI/Plenum Data Corporation, New York.

[218] Ulutan D, Özel T (2013) Determination of Tool Friction in Presence of Flank Wear and Stress Distribution Based Validation Using Finite Element Simulations in Machining of Titanium and Nickel Based Alloys. *Journal of Materials Processing Technology* 213(12):2217–2237.

[219] Ulutan D, Sima M, Özel T (2011) Prediction of Machining Induced Surface Integrity Using Elastic-viscoplastic Simulations and Temperature-dependent Flow Softening Material Models in Titanium and Nickel-based Alloys. *Advanced Materials Research* 223:401–410.

[220] Umbrello D, Filice L (2009) Improving Surface Integrity in Orthogonal Machining of Hardened AISI 52100 Steel by Modeling White and Dark Layers Formation. *CIRP Annals—Manufacturing Technology* 58(1):73–76.

[221] Umbrello D, Outeiro JC, M'Saoubi R, Jayal AD, Jawahir IS (2010) A Numerical Model Incorporating the Microstructure Alteration for Predicting Residual Stresses in Hard Machining of AISI 52100 Steel. *CIRP Annals—Manufacturing Technology* 59(1):113–116.

[222] Vaz M, Cardoso EL, Munoz-Rojas PA, Carniel TA, Leursen MA, Tomiyama M, da Silva JO, Stahlschmidt J, Trentin RJ (2015) Identification of Constitutive Parameters—Optimization Strategies and Applications. *Materialwissenschaft und Werkstofftechnik* 46(4–5):477–491.

[223] Vogler MP, DeVor RE, Kapoor SG (2004) On The Modeling and Analysis of Machining Performance in Micro-endmilling, Part I: Surface Generation. *Journal of Manufacturing Science and Engineering* 126(4):685–694.

[224] Wedberg D, Svoboda A, Lindgren LE (2012) Modelling High Strain Rate Phenomena in Metal Cutting Simulation. *Modelling and Simulation in Materials Science and Engineering* 20:085006. (19pp).

[225] Yen YC, Söhner J, Lilly B, Altan T (2004) Estimation of Tool Wear in Orthogonal Cutting Using the Finite Element Analysis. *Journal of Materials Processing Technology* 146(1):82–91.

[226] Yovanovich MM (1982) Thermal Contact Resistance. *Progress in Astronautics and Aeronautics* 83:83–95.

[227] Yovanovich MM, Burde SS, Thompson JC (1976) Thermal Constriction Resistance of Arbitrary Planar Contacts with Constant Flux. *Proceedings of the AIAA 11th Thermophysics Conference*, San Diego, CA, 1–6.

[228] Zahedi SA, Demiral M, Roy A, Silberschmidt VV (2013) FE/SPH Modelling of Orthogonal Micro-machining of FCC Single Crystal. *Computational Materials Science* 78:104–109.

[229] Zemzemi F, Bensalem W, Rech J, Dogui A, Kapsa P (2008) New Tribometer Designed for the Characterization of the Friction Properties at the Tool/Chip/Workpiece Interfaces in Machining. *Tribo Test* 14:11–25.

[230] Zemzemi F, Rech J, Bensalem W, Dogui A, Kapsa P (2007) Development of a Friction Model for the Tool-chip-workpiece Interfaces During Dry Machining of AISI4142 Steel with Tin Coated Carbide Cutting Tools. *International Journal of Machining and Machinability of Materials* 2(3/4):361–377.

[231] Zemzemi F, Rech J, Bensalem W, Dogui A, Kapsa P (2007) Identification of Friction and Heat Partition Model at the Tool-chip-workpiece Interfaces in Dry Cutting of an Inconel718 Alloy with CBN and Coated Carbide Tools. *Advances in Manufacturing Science and Technology* 38(1).

[232] Zerilli FJ (2004) Dislocation Mechanics-based Constitutive Equations. *Metallurgical and Materials Transactions A* 35(9):2547–2555.

[233] Zerilli FJ, Armstrong RW (1987) Dislocation-mechanics-based Constitutive Relations for Material Dynamics Calculations. *Journal of Applied Physics* 61 (5):1816–1825.

[234] Zhang P, Xu G, Fu X, Li C (2011) Confined Jet Impingement of Liquid Nitrogen onto Different Heat Transfer Surfaces. *Cryogenics* 51:300–308.

[235] Zhang Y, Mabrouki T, Nelias D, Courbon C, Rech J, Gong Y (2012) Cutting Simulation Capabilities Based on Crystal Plasticity Theory and Discrete Cohesive Elements. *Journal of Materials Processing Technology* 212(4):936–953.

[236] Zhou F (2014) A New Analytical Tool-chip Friction Model in Dry Cutting. *International Journal of Advanced Manufacturing Technology* 70:309–319.

[237] Zuckerman N, Lior N (2006) Jet Impingement Heat Transfer: Physics, Correlations, and Numerical Modeling. George AG, James PH, Avram BC, Young IC, (Eds.) *Advances in Heat Transfer*, 39. Elsevier. 565–631.